Micro-Physical Modeling of Aircraft Exhaust Plumes and Condensation Trails

by

Thibaud M. Fritz

Submitted to the Department of Aeronautics and Astronautics
in partial fulfillment of the requirements for the degree of

Master of Science in Aeronautics and Astronautics

at the

MASSACHUSETTS INSTITUTE OF TECHNOLOGY

June 2018

Signature redacted

Author .....
Department of Aeronautics and Astronautics
May 21, 2018

Signature redacted

Certified by .....
Steven R.H. Barrett
Associate Professor of Aeronautics and Astronautics
Thesis Supervisor

Signature redacted

Accepted by .....
Hamsa Balakrishnan
Associate Professor of Aeronautics and Astronautics
Chair, Graduate Program Committee

Micro-Physical Modeling of Aircraft Exhaust Plumes and Condensation Trails

by

Thibaud M. Fritz

Submitted to the Department of Aeronautics and Astronautics
on May 21, 2018, in partial fulfillment of the
requirements for the degree of
Master of Science in Aeronautics and Astronautics

Abstract

The ability to quantitatively assess the environmental impacts of air transport operations is necessary to estimate their current and future impacts on the environment. Emissions from aircraft engines are a significant contributor to atmospheric NO_x driving climate change, air quality impacts and other environmental concerns. To quantify these effects, global chemistry-transport models are frequently used. However, such models assume homogeneous and instant dilution into large-scale grid cells and therefore neglect micro-physical processes, such as contrail formation, occurring in aircraft wakes. This assumption leads to inaccurate estimates of NO_y partitioning, and thus, an over-prediction of ozone production. To account for non-linear plume processes, a Lagrangian aircraft plume model has been implemented. It includes a unified tropospheric-stratospheric chemical mechanism that incorporates heterogeneous chemistry. Micro-physical processes are considered throughout the entire plume lifetime. The dynamics of the plume are solved simultaneously using an operator splitting method. The plume model is used to quantify how the in-plume chemical composition is affected in response to various environmental conditions and different engine and/or fuel characteristics.

Results demonstrate that an instant dilution model overestimates ozone production and accelerates conversion of nitrogen oxides compared to the plume model. Sensitivities to the NO_x emission index have been derived and the dependence of the plume treatment on the background atmosphere mixing ratios, pressure and latitude has been investigated for a future regional scale assessment of the aviation sector. The cumulative impact of successive flights has been estimated. Contrail micro-physical and chemical properties have been computed under different scenarios.

This aircraft plume model has been extensively validated and enables an in-depth assessment of the impact of one or multiple flights on local atmospheric conditions.

Thesis Supervisor: Steven R.H. Barrett
Title: Associate Professor of Aeronautics and Astronautics

Acknowledgments

It is common practice to start the thesis acknowledgements by expressing gratitude to one's advisor for their devotion and support. I would like to expressively thank my academic advisor, Prof. Steven Barrett, who has been a constant source of assistance and inspiration throughout the past months and will remain as such for my PhD. He welcomed me to the Laboratory for Aviation and the Environment and granted me with wonderful research and academic opportunities.

I have also been greatly assisted by LAE's research scientists, Seb Eastham and Ray Speth, who gratefully shared their scientific knowledge and always guided me in the roller coaster that is life at MIT. I now know more about atmospheric chemistry more than I ever thought I would.

I would like to thank all my colleagues at the Lab for Aviation and the Environment with whom I have shared philosophical discussions on various subjects ranging from health impacts of high-altitude ammonia emissions to us asking ourselves: what really is a cloud? I would especially thank Drew for making the lab more enjoyable every day, Prashanth for being the inventive and passionate person that he is, Ines for always being social and outgoing and Kingshuk for the particularly engaged conversations we've had. I would also like to thank Akshat for his wise words that enlightened my mind many times. I am grateful to Luke, with whom I can only speak in Math and Python. Thanks to you, I have seen more contrails in one day than in my entire life.

I cannot express enough gratitude and love to Emma, with whom I have shared so many wonderful moments. I feel so blessed to have met you. Thank you for being the person I can always rely on. There will never be a day that goes by that I will not be grateful for you.

Last but not least, I am forever thankful to my parents, Laurence and Rémy, who share with me all their love, strength and wisdom. I know deep down that this journey would not have been possible without them. Merci.

Contents

List of Figures

List of Tables

Chapter 1

Introduction

In 1999, the Intergovernmental Panel on Climate Change (IPCC) released the first estimate of the global climate impact of the aviation sector corresponding to 3.5% of total anthropogenic warming for 1992 operations [33]. Following that, growing attention has been paid to the effect of aircraft emissions on the climate as aviation industry and passenger traffic has experienced rapid expansion. On average, the growth in passenger traffic was estimated at 5.3% per year for the period from 2000 to 2007 [24]. Consequently, total aviation emissions have continuously increased as demand for air transport has outpaced the reductions in emission indices [25]. Recent studies estimated the share of aviation in global anthropogenic warming to be 5% in 2005, with uncertainty bounds that extend up to 14% [24].

Aviation is a unique sector in terms of its environmental challenges because it is the only significant anthropogenic source of pollution at high altitude. 75% of the emissions from commercial flights occurred above 7 km altitude in 2006 [56]. The release of chemically reactive substances in the upper troposphere or lower stratosphere (UTLS) from aircraft exhausts induces perturbations in the environmental chemical balance that can persist for days to months. Nitrogen oxides from aircraft emissions, NO_x ($= NO + NO_2$), are formed by thermal decomposition and oxidation of N_2 in the combustor of engines. The impact of aircraft-emitted NO_x was first studied because of the potential impact that supersonic aircraft could have on the ozone layer. Since then, NO_x have been found to be among the species with the greatest potential im-

pact [33] and emissions from the subsonic fleet have been shown through numerical simulations to increase tropospheric ozone levels in the Northern hemisphere by 2 to 9% [4,38].

Global Eulerian 3-D atmospheric chemistry-transport models are the most commonly used prediction tools when studying the impacts of subsonic commercial aviation on the environment. These models assume that the aircraft exhaust is instantaneously and homogeneously mixed with ambient air in grid cells that still remain coarse relative to the plume because of computational limitations [3,10,28].

However, these large-scale models do not account for the initial high species concentrations that can be several orders of magnitude larger than their respective background values. Therefore, the impacts of the non-linear processes in the early stages of the plume are not captured in such simulations. It has been shown that solving the chemistry at the grid scale provides different results than plume-scale models [6,23,34]. Additionally, instant dilution neglects any plume-scale micro-physical processes, an important sink of water vapor and nitric acid at low temperatures and provide a surface for rapid heterogeneous chemistry.

Initial high NO_x mixing ratios in aircraft plumes lead to efficient conversion of nitrogen oxides to reactive nitrogen compounds, NO_y, which diminish the potential of aviation emissions to form ozone. To account for these non-linear chemical processes, a parameterized plume model has been implemented. This sub-grid plume representation combines gas-phase chemistry, entrainment of ambient air and micro-physical processes.

Among aviation's environmental impacts, condensation trails and aircraft-induced cirrus clouds are the most important and yet most uncertain sources of radiative forcing [24]. Even if the thermodynamic conditions required for contrail formation are well understood [1,37], the level of scientific understanding of the micro-physical pathway leading to their formation and their impact on the in-plume chemistry is still low.

Field measurements over the past decades, e.g. SUCCESS [47], POLINAT [43] and the SULFUR experiments [40], have investigated contrail ice crystals and liquid

aerosols characteristics and, as a result, models have been built to study aerosol formation and growth in aircraft plumes. Parametric studies have been carried out and have found that ambient relative humidity, fuel sulfur contents and soot number emissions are key parameters affecting contrail formation and particle growth [22], [57]. In the early stages, non-volatile aerosols take up a significant amount of the emitted water vapor through condensation and heterogeneous freezing, potentially leading to persistent contrails, and liquid aerosols form. During the plume expansion regime, gas species react and diffuse, aerosols undergo coagulation and they affect gaseous species concentrations through heterogeneous chemistry on their surface.

The development of the biofuel industry has been identified as a potential opportunity to reduce aviation's climate impact and CO_2 burden. Additionally, the use of alternative jet fuels instead of conventional fuel has the property of greatly decreasing soot and sulfur emissions. This paper presents how different emission indices, through the use of different fuels, can influence the micro-physical characteristics and the in-plume gas-phase chemistry.

1.1 Thesis synopsis

This work aims to assess the impact of modeling non-linear chemical mechanisms in an expanding aircraft exhaust plume as compared to a grid scale model. The present study addresses the question: Does the inclusion of small-scale plume processes alter the local and global results, as resolved by a global chemistry-transport model (CTM)?

Because of computational limitations, global CTMs still have relatively coarse grid cells compared to an aircraft plume that usually widens up to a few kilometers. Therefore, global CTMs cannot accurately describe the small-scale chemical and micro-physical processes in an aircraft plume. To answer this lack of detailed plume-scale models, an aircraft exhaust model has been developed. This model includes an accurate chemical integrator with a comprehensive set of chemical reactions and micro-physical processes.

1.2 Previous work on aircraft plume modeling

Several aircraft plume parameterizations have been developed to quantify the non-linear chemical processes that occur in the exhaust of an aircraft [23,27,34,54]. These models use the assumption that the dispersion of an aircraft wake can be accurately modeled using a Gaussian plume model. This representation assumes that the plume growth is set by turbulent diffusion parameters and a shear coefficient. This assumption is theoretically only valid for non-reactive species. Temporal variations in photochemistry and spatial variations due to non-linearities can cause the concentration profiles to not be Gaussian and even asymmetric in the presence of ice crystals.

In the present model, diffusion is coupled to a comprehensive chemistry model and detailed micro-physical processes.

To the author's knowledge, no such aircraft plume model includes detailed micro-physical processes to model the effect of contrails on in-plume chemistry through heterogeneous reactions on the surface of ice crystals.

Chapter 2

Methods

In order to assess the effect of the plume-scale dynamical and chemical processes on aircraft exhausts, the Aircraft Plume Chemistry, Emissions and Micro-physics Model (APCEMM) has been developed. A plume-scale treatment of aircraft emissions is necessary to account for the non-linear chemistry in the aircraft wake. After their release in the atmosphere and during the diffusion phase, the species concentrations in the aircraft plume can be several orders of magnitude larger than their background levels. NO_x concentrations at cruise altitude can reach values up to 20 ppbv in the early stages of the plume, whereas background NO_x levels are typically between 0.007 ppbv and 0.15 ppbv in flight corridor such as the North Atlantic Flight Corridor (NAFC) [42]. Non-linearity in the chemical rates means that in-plume chemistry does not necessarily behave identically to the surrounding atmosphere.

The growth and chemical evolution of a single aircraft plume are modeled using an Eulerian-Lagrangian approach. Chemical concentrations and aerosol characteristics are treated by tracking a cross-section of the plume, perpendicular to the flight path. This cross-section is discretized in a finite number of fixed concentric elliptic rings, allowing the model to account for dilution over time. Chemistry is solved in each ring and at every time step using an operator splitting method. Micro-physical processes are also considered.

Aircraft wakes can be thought of as a succession of three distinct regimes (Figure 2-1). In the near field, compressibility effects arise from the momentum-driven jet

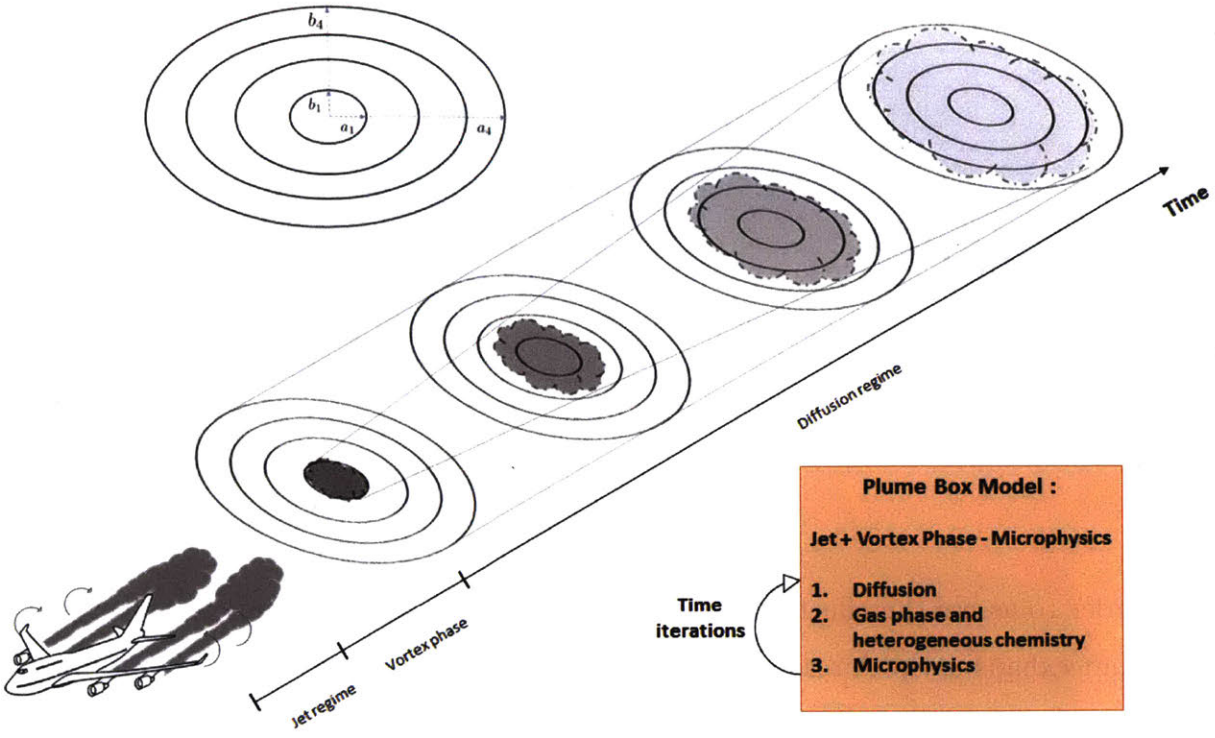

Figure 2-1: Sketch and modeling of a Lagrangian plume tracking approach in stationary constant-area rings. The rings' major and minor axis are denoted by a_i and b_i respectively.

that last for a short amount of time of the order of a few seconds. During this regime, the vorticity lines, that form around the wing tips because of a span-wise variation in sectional circulation, start to roll up into counter-rotating vortices and move downwards because of their mutually induced velocity and entrain the plume. The force balance between the vortex motion and the inertial force induced by the momentum excess at the engine exit induces a sinking motion of the wake. Viscous dissipation of turbulent energy in ambient air causes the vortices to break apart leading to the diffusion regime. In this regime, the plume then expands in ambient air once aircraft-induced effects have vanished. Diffusion parameters are controlled by the vertical stratification of the atmosphere and shear forces. Typical timescales and dilution ratios for an aircraft plume are shown in Table 2.1.

Initially, the plume is hot and undergoes cooling leading to a spike in ice and liquid water saturations roughly 10 ms after emission, triggering a wide range of

Table 2.1: Plume timescales and dilution ratios

	Aircraft Plume Chemistry, Emissions and Microphysics Model			
	Early-plume model			Long-term plume model
Phases	Early Jet Regime	Jet Regime	Vortex Regime	Diffusion Regime
Timescale	0.1 s	10 s	100 s	Few hours up to a day
Dilution ratio at end of phase [-]	5.5×10^{-1}	2.6×10^{-3}	9.9×10^{-4}	$< 1.0 \times 10^{-4}$

micro-physical processes. During this initial jet regime, formation of sulfate aerosols, freezing on solid nuclei, condensation, heterogeneous nucleation and coagulation occur. Previous studies have suggested that homogeneous freezing is unlikely in aircraft plumes given the large number of pre-existing nuclei [57]. This behavior can be explained because combustion particles can acquire an ice coating at temperatures much warmer than cruise temperatures, therefore implying that ice crystals formed in the vicinity of the engines freeze because of heterogeneous nucleation. This indicates that ice formation occurs on soot particles earlier than predicted by the homogeneous nucleation theory. Therefore, freezing through homogeneous nucleation is not considered in this work.

The general transport equation of a compressible gas in conservation form can be written as:

$$\frac{\partial \rho Y_k}{\partial t} + \nabla \cdot (\rho Y_k \mathbf{u}) = -\nabla \cdot (\boldsymbol{\xi}_k) + \dot{\Omega}_k, \tag{2.1}$$

where Y_k, ρ, $\mathbf{u}$ and ξ_k are the vapor mass fraction of species k, the gas density, the velocity field and the diffusion flux of species k, respectively. $\dot{\Omega}_k$ represents any source or loss term associated with chemical or micro-physical processes for species k.

By switching to a time-dependent Lagrangian reference frame, we introduce the

material derivative and the conservation equation for the scalar field Y_k becomes

$$\frac{D\rho Y_k}{Dt} = -\nabla\cdot(\boldsymbol{\xi}_k) + \dot{\Omega}_k. \tag{2.2}$$

The Aircraft Plume Chemistry, Emission and Micro-physics Model groups up the jet and vortex phases into a box model assuming a top-hat distribution in the plume. The output of this box model is then fed to the finite-volume Lagrangian model that deals with the long term diffusion regime.

2.1 Modeling of the jet and vortex regimes

In the jet and vortex regimes, we adopt a formulation similar to the box model used in Kärcher et al. [19]. The rate of change of the molecular concentration is dominated in this regime by turbulent mixing. The contribution of wake mixing in equation (2.1) is approximated as a first-order decay term proportional to a time-dependent entrainment rate $\omega_C(t)$, i.e.

$$\left(\frac{DC_k}{Dt}\right)\Big|_{\text{mix}} = -\omega_{C_k}(t)(C_k - C_{\text{Amb},k}), \tag{2.3}$$

where C_k is the molecular concentration of species k.

This entrainment rate agrees with the experimental data and curve fit provided in Schumann et al. [42] for times greater than 1 s. In equation (2.3), $C_{Amb,k}$ is the ambient molecular concentration of species k and is assumed to be constant during the jet and vortex regimes considering that the timescale associated with the gas-phase chemistry is much greater than the time at which the diffusion regime starts. Similarly we assume that, during this regime, gas-phase chemistry does not influence the species concentrations along the plume axis except for the conversion of S(IV) to S(VI) and NO_x to HNO_2 and HNO_3, which evolve on similar timescales due to high initial concentrations.

Entrainment of gaseous species and mixing of cold air with the hot exhaust stream are assumed to be identical since experiments from Forstall et al. [12] have shown that

typical Lewis numbers are close to unity in coaxial jets, such as aircraft plumes.

The downward motion induced by the wing tip vortices causes the air to heat up adiabatically, independently of the local lapse rate [52]. The plume temperature evolution is expressed as the sum of a positive heating due to vortex sinking and a first-order decay term, representing entrainment, i.e.

$$\frac{dT_p}{dt} = \Gamma_d v_z - \omega_T(t)(T_p - T_{\text{Amb}}(z)), \tag{2.4}$$

where T_p is the plume temperature, Γ_d the adiabatic lapse rate, v_z the vertical velocity of the plume and T_{Amb} the ambient temperature which depends on the ambient lapse rate, which was obtained as a function of latitude and altitude from monthly-averaged GEOS meteorological data. The plume acquires a vertical motion during the vortex regime, such that v_z is assumed to be non-zero only between the time at which the vortices start inducing a vertical displacement of the plume and the vortex break-up time. The wake vortex sinking is computed according to a model from Schumann [39]. A parametric formulation is used to estimate the mean downward displacement as a function of aircraft and ambient atmospheric characteristics.

In the early stages of the plume, oxidation of NO and NO_2 results in the formation of HNO_2 and HNO_3. Similarly, S(IV) undergoes oxidation to gaseous S(VI). As described by Kärcher et al., conversion efficiencies of NO, NO_2 and SO_2 depend greatly on the exit plane hydroxyl radical concentration [21]. In their work, Tremmel et al. inferred initial OH concentrations at the combustor and engine exit through measurements of NO, HNO_2, HNO_3 as well as CO_2 to account for plume dilution [48]. Their results indicate that the OH emission index ranges between 0.32 and 0.39 g (kg fuel)$^{-1}$ for the JT9D-7A, which corresponds to an engine exit mixing ratio lying between 9.0 and 14.4 ppmv. Conversion efficiencies used in our model are depicted in Table 2.2. Even though the conversion efficiencies remain of the order of a few percents, they are monotonically increasing with the OH engine exit mixing ratio, as more radicals are available for the following reactions.

$$\begin{aligned} NO + OH &\rightarrow HNO_2 \\ NO_2 + OH &\rightarrow HNO_3 \\ OH + OH &\rightarrow H_2O_2 \end{aligned} \tag{2.5}$$

Table 2.2: Assumed conversion efficiencies of NO_x and SO_2 to secondary species at the end of the vortex regime

NO	$\rightarrow$	HNO_2	1.5%
NO_2	$\rightarrow$	HNO_3	4.0%
SO_2	$\rightarrow$	H_2SO_4	0.5%
OH	$\rightarrow$	H_2O_2	2.0%

As the plume cools down and mixes with ambient air, micro-physical processes contribute to modifying the in-plume mixing ratios. The rate of change of C_k due to micro-physics can be further divided into

$$\begin{aligned} \left(\frac{DC_k}{Dt}\right)\Big|_{\text{Micr}} = \left(\frac{DC_k}{Dt}\right)\Big|_{\text{Freez}} + \left(\frac{DC_k}{Dt}\right)\Big|_{\text{Cond}} \quad \cdots \\ + \left(\frac{DC_k}{Dt}\right)\Big|_{\text{Nucl}} + \left(\frac{DC_k}{Dt}\right)\Big|_{\text{Coag}}, \end{aligned} \tag{2.6}$$

where the terms respectively stand for freezing, condensation, nucleation and coagulation. These terms represent micro-physical processes that govern the formation and evolution of liquid and solid particles in the aircraft wake as well as uptake of gaseous species.

The micro-physical model is adapted from the work by Kärcher [22]. It uses a sectional approach to track ice crystals and condensation nuclei in discretized bins. Tracking all particles for modeling contrail formation would require massive computational power since soot emission indices usually range from 10^{15} to 6×10^{16} kg fuel^{-1} [55].

Solid nuclei, soot and metal particles, emitted by the aircraft serve as condensation nuclei for water vapor. Under supersatured conditions, deposition and sublimation induce ice crystal growth, deplete gaseous water vapor and increase the ice water

content. Ice crystals are treated as a mono-disperse distribution and are assumed spherical. Because of relatively low ambient temperatures, water that condenses is assumed to freeze instantaneously, therefore the ice crystals essentially grow by deposition of water molecules onto their surface. The instantaneous change in the ice mass of a particle, m_p, is given by

$$\frac{dm_p}{dt} = H_p^{\text{act}}(m_p) \times 4\pi C_p D_{\text{v,eff}} \left(P_{\text{H}_2\text{O}} - P_{\text{H}_2\text{O}}^{\text{sat}}\right), \tag{2.7}$$

where C_p is the ice crystal capacitance (equal to the particle radius r_p for spherical nuclei) and P_{H_2O} the water partial pressure. $D_{\text{v,eff}}$ is the effective water vapor diffusion coefficient in air and accounts for latent heat effects calculated from

$$D_{\text{v,eff}} = \frac{D_{\text{v}} \times \beta(r_p)}{\frac{D_{\text{v}} L_s P_{\text{H}_2\text{O}}^{\text{sat}}}{\kappa_d T}\left(\frac{L_s}{R_{\text{v}} T}\right) + R_{\text{v}} T}, \tag{2.8}$$

where L_s is the latent heat of sublimation and κ_d the thermal conductivity of air. The function β accounts for the transition of the uptake from the gas kinetic ($Kn \gg 1$) to the diffusional regime ($Kn \to 0$), and

$$\beta(r_p) = \left(\frac{1}{1 + r_p/\lambda_v} + \frac{2 D_{\text{v}} C_p}{\alpha v_{\text{th,v}} r_p^2}\right)^{-1} \tag{2.9}$$

with α being the deposition coefficient. For deposition of water molecules on ice particles, we take $\alpha = 0.5$ which is in agreement with laboratory and field studies [13]. The mean free-path of vapor molecules λ_v and the diffusion coefficient of vapor in air D_v are functions of the local temperature and pressure and are computed according to relations from Pruppacher et al. [36].

Activation of solid nuclei is characterized through the variable H_p^{act}, as described by Picot [35]. It assumes that the lower bound for particle shrinking is the dry soot core radius, $r_p = r_{\text{soot}}$, which corresponds to a zero ice mass. Additionally, soot nuclei can only get activated with an ice coating under supersaturated conditions, i.e. if the

relative humidity with respect to liquid water is greater than unity, locally:

$$H_p^{\text{act}} = \begin{cases} 1 & \text{if } m_p > 0 \text{ or } \text{RH}_{w,\text{loc}} \geq 1 \\ 0 & \text{otherwise} \end{cases} \tag{2.10}$$

The Kelvin effect accounts for the nucleus curvature effects and raises the apparent vapor pressure over a convex surface relative to a flat surface. The correction term appears in equation (2.7) through the saturation pressure $P^{\text{sat}}_{\text{H}_2\text{O}} = \exp(r_K/r_p) \times P^{\text{flat}}_{\text{H}_2\text{O}}$, where r_K is the Kelvin radius and $P^{\text{flat}}_{\text{H}_2\text{O}}$ is the saturation vapor pressure over a flat surface and is purely a function of temperature [36].

Similarly, condensation of sulfuric acid and nitric acid on soot and ice crystals can occur in an aircraft plume and form partial liquid coatings on their surface. As the plume cools down below 300 K, the saturation vapor pressure of sulfuric acid drops so low that all sulfuric acid can be considered in liquid form (either as liquid droplets or as liquid particle coatings). In comparison, H_2O and HNO_3 in liquid form can evaporate, under subsaturated conditions, as the saturations tend to ambient values. The growth of the liquid layer on solid particles is related to the condensation (or evaporation) rate of H_2O, H_2SO_4 and HNO_3

$$\begin{aligned} \frac{dN_{k,p}}{dt} = 4\pi r_p D_k \beta(r_p) \left(\frac{P_k - P_k^{\text{sat}}}{k_B T} \right) \quad \cdots \\ \times (1 + \delta(p - s)(\theta - 1)) \end{aligned} \tag{2.11}$$

where $N_{k,p}$ is the number of molecules of type k on a particle of type p, D_k the gas diffusivity, P_k and P_k^{sat} the partial and saturation pressures of species k, respectively. The index s stands for soot particles. θ describes the surface coverage of the particle liquid coating. The model accounts for condensation of molecules on the surface with a liquid coating. For soot particles, the rate of change of the mass of condensed species directly scale with the surface coverage but this assumption does not hold for other types of aerosols [22]. Therefore, the Delta-function, introducing the dependency on θ, vanishes for non-soot particles. For heteromolecular condensation, deposition coefficients are usually determined experimentally but their range of uncertainty remain

significant [36]. Values similar to the work from Kärcher [22] are used in this model. Gas diffusivities for H_2SO_4 and HNO_3 are taken from Tang et al. [46].

The nucleation model is used to predict binary homogeneous and heterogeneous nucleation rates in the aircraft wake. Over the past decades, several nucleation parameterizations have been established to study binary homogeneous nucleation in a sulfur-rich environment [17, 30, 53]. Jung et al. [18] has computed different sensitivities using these models and provided further validation of the models cited previously, comparing the results to field measurements. Given the range over which ambient conditions (relative humidities, sulfur concentration, ambient temperature) can vary in an aircraft plume, we have chosen to follow the parameterization from Vehkamäki et al. [53]. Even though their model is only valid between 230.15 K and 305.15 K, we expect sulfate aerosols to form before the plume reaches the lower bound of the temperature range. In addition to the parameterized nucleation rate, their model also provides critical cluster size and composition.

Previous studies have investigated the freezing behavior of sulfate aerosols and liquid sulfur soot coating at low temperatures [44]. In his model, Tabazadeh et al. [45] found that sulfate aerosols are able to freeze but an ice supersaturation of about 1.5 at 210 K is required. Kärcher showed that freezing of sulfuric acid tetrahydrate (SAT) is extremely unlikely under typical plume conditions [20]. Therefore, our model does not account for freezing of sulfate aerosols, as in the model from Wong et al. [57].

Additionally, we also consider unary nucleation of gaseous water and binary heterogeneous $H_2O - H_2SO_4$ nucleation. As described by Zhao et al., peak supersaturations in an aircraft plume are more than an order of magnitude lower than the threshold to allow water to nucleate homogeneously [58]. Unary heterogeneous nucleation is far more likely since the presence of a nucleus reduces the formation enthalpy of a germ on the particle surface [11, 36].

Coagulation of aerosols occur when particles collide and stick to each other. Coagulation is a volume-conserving phenomenon. Assuming that shattering and breakup are negligible, coagulation decreases the number of particles but increases their size, leading to a lower surface area. The work from Beard et al. and numerical simulations

from Jacobson have concluded that breakup is of importance for particles larger than 100 μm in diameter [2, 16]. However, coalescence efficiencies essentially converge to unity when the particle diameter is smaller than 14 μm. Since aerosol sizes rarely exceed this threshold over the plume lifetime, we neglect droplet breakup and particle shattering.

The plume aerosol population consists of aircraft-produced and entrained ambient aerosols that can interact through coagulation. Sulfate aerosols are assumed to be distributed log-normally, while soot and ice particles are considered monodisperse. The general equation governing the temporal evolution of the aerosol number density of size $[r_k, r_{k+1}]$ is

$$\frac{dn_k}{dt} = \frac{1}{2}\sum_{j=1}^{k-1} K_{j,k-j} n_j n_{k-j} - \sum_{j=1}^{+\infty} K_{k,j} n_k n_j, \tag{2.12}$$

where n_k is the number density of particles in bin k and K is the coagulation kernel which represents the physics of the problem. Equation (2.12) states that the rate of change in the number density in bin k corresponds to the rate at which smaller particles of size $k - j$ coagulate with particles of size j minus the rate at which the particles of size k are lost due to coagulation with particle of all sizes.

Coagulation of newly-formed aerosols and scavenging by soot and ice particles take place on different timescales. Among the different mechanisms considered, Brownian coagulation, sedimentation-induced aggregation and turbulence-driven coagulation, the former is the dominant mechanism by several few orders of magnitude below 0.5 μm. The coagulation timescale of particles of radius r_1 can be evaluated from $t_{\text{coa}} = 1/(K(r_1, r_2)n_2)$, where n_2 and r_2 are the number density and the radius of the scavenging particles. Figure 2-2 depicts the approximate coagulation timescales as a function of the number density n_2 and radius r_2. These timescales are obtained assuming monodisperse distributions for the scavenging particles (of size r_2) and scavenged particles (of size r_1).

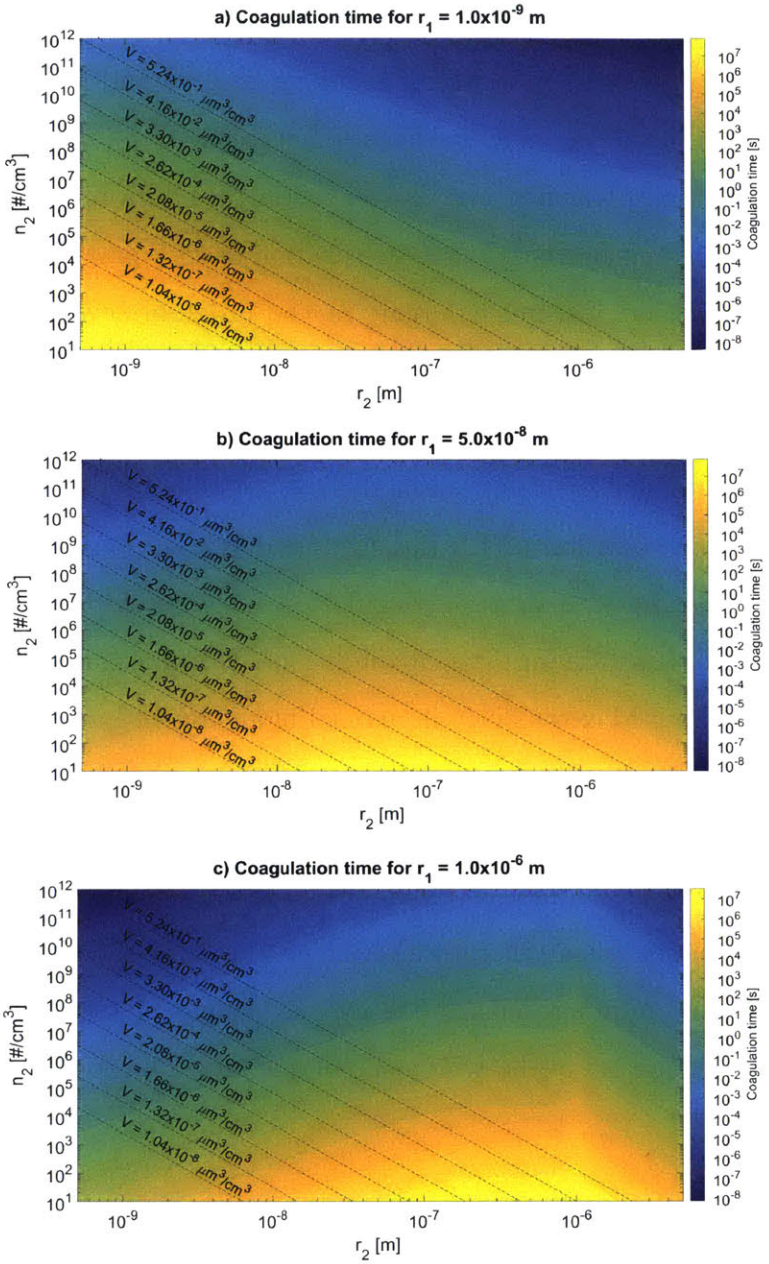

Figure 2-2: Approximate coagulation timescales versus the radius and the number density of the scavenging particles, assuming a scavenged particle radius of r_1 = 1 nm, 15 nm, 1 μm (from top to bottom). Dashed lines represent constant aerosol volume. The coagulation kernel considers Brownian coagulation, turbulence and sedimentation-induced coagulation phenomena. A pressure of 240 hPa and a temperature of 220 K were assumed.

Self-coagulation of sulfate aerosols (r_1 = .5 - 10 nm) occurs on a timescale of a

few seconds to minutes (Figure 2-2 a)), assuming a typical number density between 10^6 and 10^{10} molecules/cm^3. Similarly, scavenging by soot and ice particles happens over timescales that are of the same order of magnitude, assuming a radius of 50 nm (1 μm) for soot particles (for ice crystals, respectively) and a number density of 10^3 molecules/cm^3. On the other hand, self-aggregation of soot particles and ice crystals occur on timescales that are much larger, of the order of several hours. We can therefore assume that coagulation and scavenging of newly formed sulfate aerosols is an important process while aggregation of soot particles and ice crystals can be neglected for the timescales considered in this early-plume model.

Instead of solving equation (2.12) directly for every size bin, which turns out to be computationally expensive, aerosol coagulation is computed using a semi-implicit, non-iterative, volume-conserving and unconditionally stable numerical scheme [15]. This model has been used extensively in aerosol modeling and aircraft plume simulations [32].

The model runs for the time required for particle size and molecular uptakes to reach a steady-state. Entrainment of ambient air into the plume decreases the aerosol volume per unit volume of air therefore reducing the potential of coagulation. The steady-state radii and number densities as well as the gas-phase mixing ratios at the end of the vortex regime are evaluated as the plume moves on to the diffusion regime.

2.2 Diffusion regime

The computational domain is discretized into a set of fixed concentric elliptical rings in which the plume expands and the chemical species react, as described in Figure 2-1. Each ring is further discretized into a lower and upper half-ring to account for temperature differences, due to the ambient lapse rate, and sedimentation of ice crystals.

In the diffusion regime, the expansion of the plume is anisotropic because of atmospheric stratification and shear stresses. Their impact on the diffusion coefficients depend strongly on the Richardson number [8]. Additionally, atmospheric stratifica-

tion counterbalances the vertical motion of the plume such that the vertical diffusion coefficient is usually much lower than the horizontal coefficient [42]. Diffusion parameters are usually estimated in situ from either measurements of dissipation rates or from vertical velocity variance [41]. Dürbeck et al. found that, for Richardson numbers above unity, diffusion coefficients lie in the range 15 $m^2/s \leq D_h \leq 23$ m^2/s and 0.15 $m^2/s \leq D_v \leq 0.18$ m^2/s [8], which agree with measurements from Schumann et al. [41].

Statistical analysis from GEOS meteorological data for the year 2015 was performed using wind velocity and temperature profiles to derive diffusion coefficients in the free atmosphere. The Richardson number was computed from the wind shear and the Brunt-Väisäla frequency and the vertical turbulent diffusivity was estimated following the approach from Schumann et al. [41]. It is worth mentioning that the model used provides an upper bound as it overpredicts the diffusion parameter at large Richardson number. The probability distribution function of the Brunt-Väisäla frequency, Richardson number and the vertical diffusion parameter are plotted in Figure 2-3 for different pressure levels. As shown in Dürbeck et al., the Brunt-Väisäla distribution is unimodal in the troposphere and peaks around $N = 0.01$ s^{-1} [8]. A second mode appears in the stratosphere at approximately around $N = 0.02$ s^{-1}. Some further analysis shows that 90% of the distribution lies at Richardson number greater than 5 indicating a weak and/or fast decaying turbulence. The vertical diffusion coefficient distribution shows two distinctive patterns. The tropospheric distribution is unimodal whereas two modes appear in the stratosphere. The distribution and its support agree with the values described by Schumann [41] and the mean values lie in the range given by Dürbeck [8].

To account for initial turbulence phenomena, the vertical diffusion parameter is modified to 1.1 m^2/s from the start of the regime to 13 minutes, as in the work from Kraabøl [23].

The diffusion flux in direction i is given by Fick's law, $\xi_{ik} = -\rho D_i \frac{\partial Y_k}{\partial x_i}$, where D is the diffusion vector. D is the sum of molecular diffusion and turbulent diffusion. However, in practice, molecular diffusion is negligible for aircraft plumes [12].

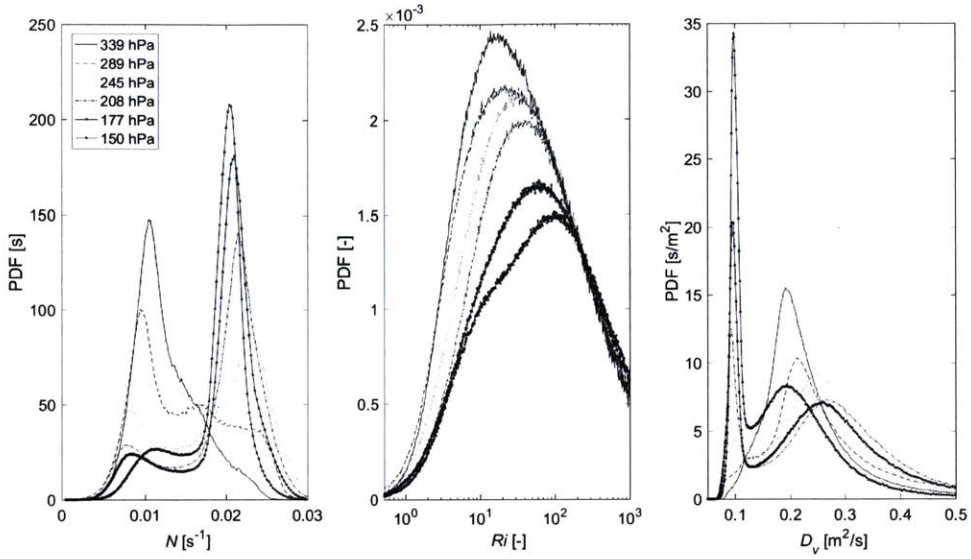

Figure 2-3: Probability density functions of the Brunt-Väisäla frequency (left), Richardson number (middle) and vertical diffusion parameter (right).

Since the plume moves at a speed much lower than the local speed of sound, we assume that the flow is incompressible, and thus, when rearranging, we end up with

$$\frac{DC_k}{Dt} = \nabla \cdot (\mathbf{D} \nabla C_k) + \dot{\omega}_k \tag{2.13}$$

The second term of the right hand side includes the chemical and micro-physical sources of all reactions for species k. It can be written as

$$\dot{\omega}_k = \sum_{i=1}^{N_{\text{reac}}} \Delta\nu_{k_i} K_i \prod_{j=1} C_{k_{i_j}}^{\nu_{k_{i_j}}} + \left(\frac{DC_k}{Dt}\right)\Big|_{\text{Microphysics}}, \tag{2.14}$$

where k_{i_j} are in the indices of the species involved in reaction i. K_i is the chemical rate of reaction i and $\Delta\nu_{k_i}$ is the difference between the forward and the backward stoichiometric coefficients.

The gas-phase chemistry mechanism is taken from the work of Eastham [9]. Heterogeneous halogen, N_2O_5 and HO_x chemistry as well as formation and evaporation of polar stratospheric clouds (PSC) and liquid binary sulfate aerosols are considered in this model. Due to their long lifetimes, reactions involving CFCs and HCFCs have

been neglected. Additionally, sea-salt aerosols are not considered in this study. The set of chemical reactions is solved numerically with KPP, which uses the sparsity of the Jacobian matrix combined with efficient integration methods to further improve the computational efficiency [7].

As the plume expands, the ice crystal size distribution changes due to growth, evaporation, gravitational settling and coagulation. Growth and evaporation are driven by the local relative humidity. Heterogeneous chemistry on ice crystals is performed using the distributions' mean quantities.

Particle growth is treated using a full-stationary size structure. Ice particles grow by advecting across diameter space to a larger size bin. The distribution function convects towards larger diameters according to the aerosol continuity equation

$$\left(\frac{\partial n}{\partial t}\right)\Big|_{\text{Growth}} = -\frac{\partial\left(gn\right)}{\partial r}, \tag{2.15}$$

where g represents the advection speed in diameter space, which equals the temporal derivative of the ice particle radius, taken from Equation 2.7, evaluated in each bins. Ice crystal growth modifies the particle volume but leaves the number of particles constant. Evaporation mechanisms, on the other hand, lead to a loss of ice crystals and act as a source of water vapor, modifying the cell's relative humidity. The extent of evaporation is limited by the size of the droplet cores. The model assumes that ice crystals in lower bins evaporate first.

Aggregation of ice particles uses the same algorithm as described previously for sulfate aerosols. The kernel includes Brownian motion, sedimentation and turbulence-driven coagulation phenomena.

Gravitational settling causes the ice particles to fall vertically, transitioning from an upper ring to one of its lower rings. Ice particle terminal velocities are computed according to Stokes law, accounting for the slip correction [36].

In solving the coupled set of equations, we use the method of operator splitting which allows us to treat the chemical kinetics terms separately from the turbulent diffusion terms and to apply optimized solution methods for these different processes.

In the literature, the plume lifetime has various definitions [31]. We have chosen to implement a fixed plume lifetime of 24 hours, which means that, given our choice of diffusion parameters, 99.2% of the exhaust mass is incorporated in the model.

2.3 Atmospheric background and initial conditions

Atmospheric background conditions are obtained from a single run, including chemistry only, with a spin-up time of 5 days. Background integration is carried on until the prescribed emission time. We do not include atmospheric transport in this study and we therefore assume that species advection at the regional scale has a limited effect on the background ambient conditions for the period considered. Different background conditions are considered in this study, depending on the emission time and the geographical location of the flight.

Initial conditions were set to background ambient conditions, except in the most inner ring where emissions from a B-747 aircraft were added. Baseline emission indices and emission parameters are listed in Table 2.3.

Table 2.3: Baseline emission indices

Species	EI	Units
CO_2	3150	g/kg_{fuel}
H_2O	1260	g/kg_{fuel}
NO_x	14	g/kg_{fuel}
CO	1.5	g/kg_{fuel}
SO_2	1	g/kg_{fuel}
Unburnt HC	0.6	g/kg_{fuel}
Soot	0.04	g/kg_{fuel}
Density	2.0	g/cm^3
Radius	20	nm

Chapter 3

Results

Aviation's climate, health and environmental impacts are directly linked to its emissions. Predicting a single flight's perturbations on its local background environment (in terms of species mixing ratios and aerosols' micro-physical properties) is thus crucial. Therefore, the focus of this section is directed towards specific metrics linked to plume chemistry and contrail properties. Regional and global-scale models commonly use a single box parameterization to handle ground-level and airborne emissions. This section aims to justify the inclusion of an aircraft plume model in a regional and global-scale chemistry transport model to study aviation's overall impact and to identify potentials pathways to lessen the environmental footprint of an individual flight. The outputs from a box model are compared with the aircraft plume model presented in the previous section.

3.1 Limitations of the Single Box Model

In the single box model, the aircraft exhaust is released uniformly and instantaneously within the grid cell. The time series of the O_3 and NO_x perturbations resulting from the emissions are shown in Figure 3-1, as computed first with a single box model and then with APCEMM. Results are shown for an emission time of 8:00 AM local time. The black dotted line represents the total nitrogen perturbation released into the system, which is a conserved quantity. The shaded area corresponds to nighttime.

Pressure and temperature were set to 240 hPa and 210 K, respectively.

The initial high nitric oxide (NO) mixing ratio leads to ozone titration, producing nitrogen dioxide (NO_2). During daytime, the latter is in turn photolyzed, freeing up a highly-reactive singlet atomic oxygen, leading to ozone production.

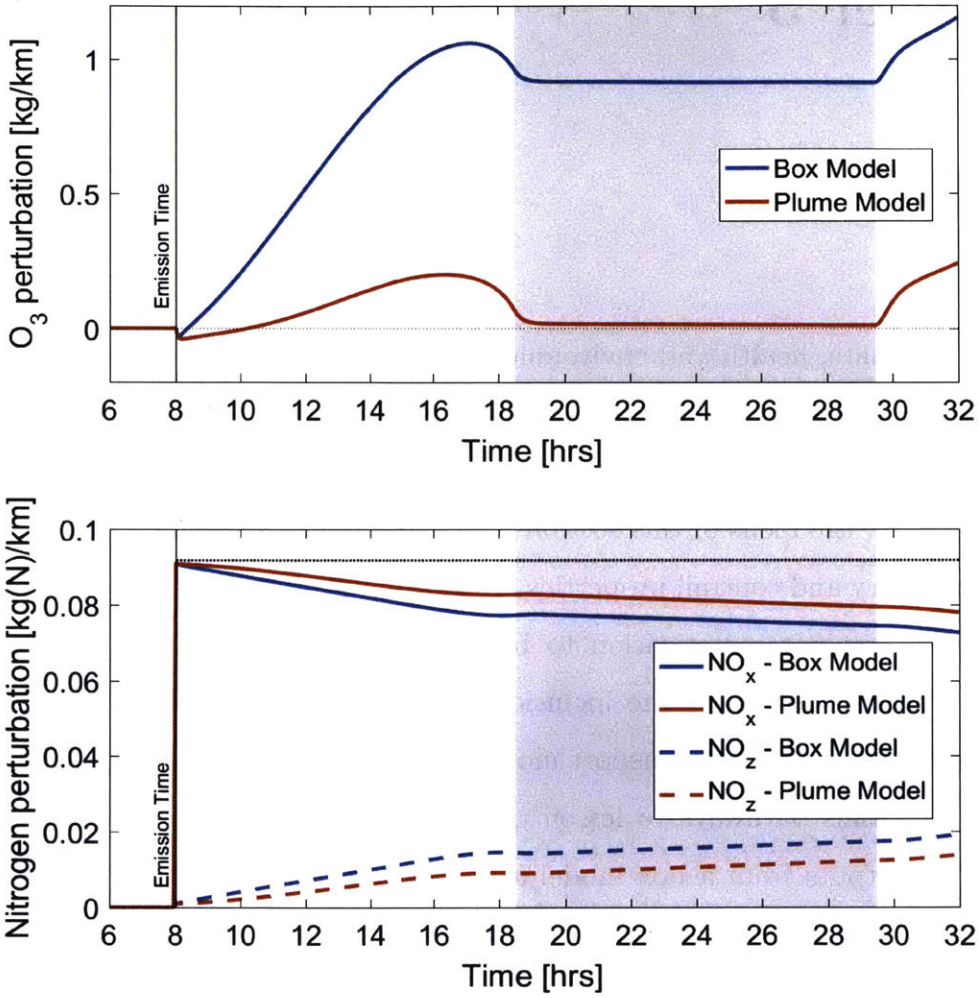

Figure 3-1: Perturbations in ozone (O_3), nitrogen oxides (NO_x) and the nitrogen reservoir species (NO_z) according to simulations using a single box model and the plume model. Shaded regions represent nighttime.

Figure 3-2 depicts secondary nitrogen species, CO and CH_4 perturbations for both models over 24 hours after emissions. Continuous and dashed lines represent results from the plume and box models respectively.

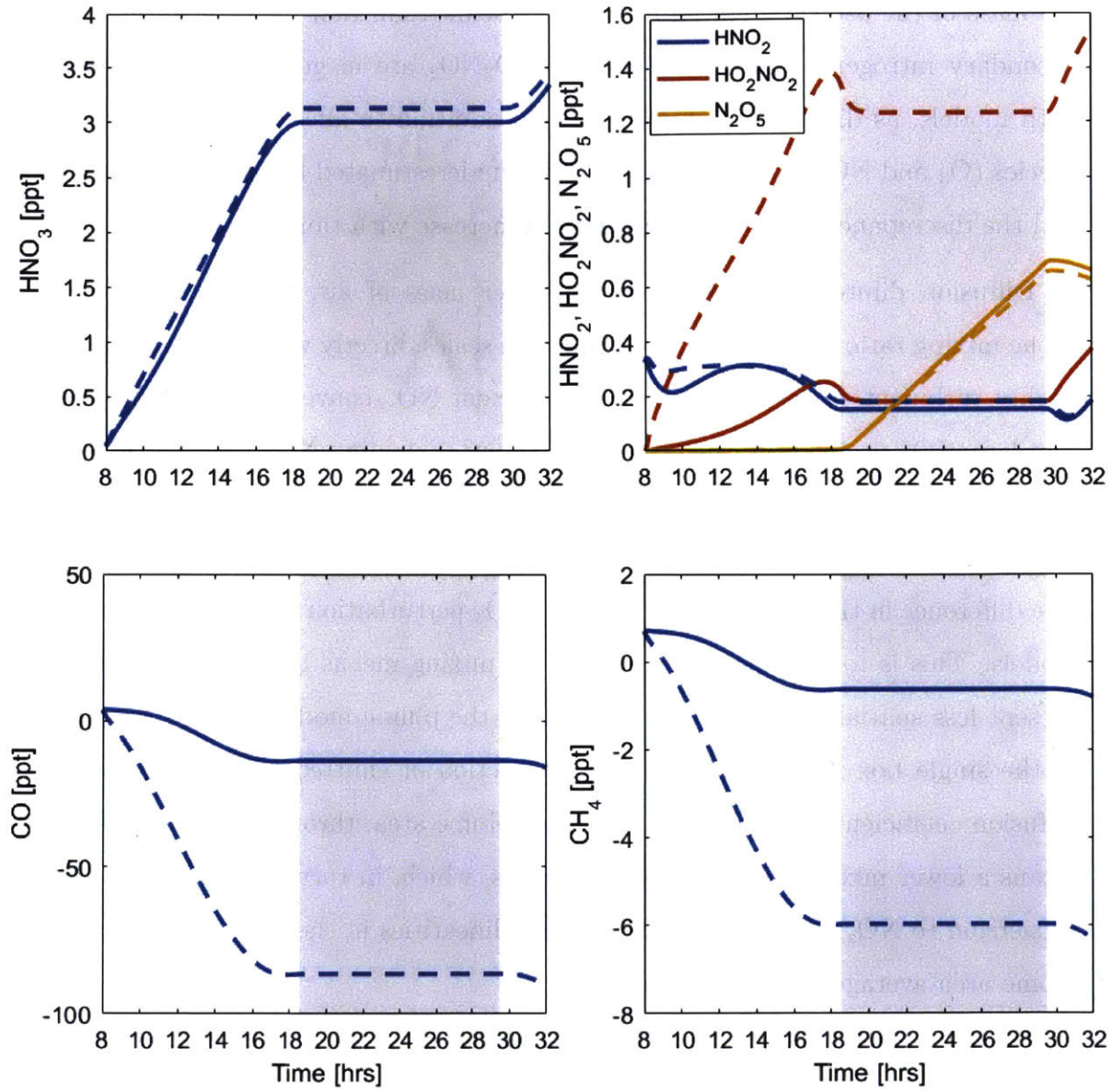

Figure 3-2: Same as Figure 3-1 but with secondary nitrogen species, CO and CH_4

The results from the aircraft plume model differ from the box model. First, the plume treatment causes the initial ozone destruction to be greater because the initial plume size is much smaller, yielding larger mixing ratios. In the single box model, ozone destruction (through NO titration) is small and can be offset shortly after emission by ozone production through NO_2 photolysis. Accordingly, in APCEMM,

the mass of the ozone perturbation remains below than that of the grid-scale ozone. Secondary nitrogen species, except from HO_2NO_2 are in good agreement between both models, as displayed in Figure 3-2. In addition to affecting the main reactive species (O_3 and NO_x), CO and CH_4 are also underestimated by the single-box model and the discrepancies between both models increase with time.

Diffusion dilutes the plume with a larger mass of air, therefore lowering the ozone mixing ratio but total ozone production scales directly with mixing parameters. Highly turbulent plumes allow for more efficient NO_x conversion, therefore leading to a larger O_3 production rate. Table 3.1 shows remaining NO_x after 24 hours, as a fraction of emitted NO_y for different mixing scenarios. The results for the box model are shown in the last row. As the plume diffusion parameter is increased, the absolute difference in the remaining NO_x and the O_3 perturbation decreases between both models. This is to be expected, as enhanced mixing means the plume mixing ratios present less spatial non-uniformity, and thus, the plume model leads to results close to the single box model. The remaining fraction of emitted NO_x decreases as the diffusion coefficients are increased. A larger plume area, through enhanced diffusion, means a lower mixing ratio of nitrogen oxides, which, in turn, leads to less chemical conversion to NO_z (= NO_y - NO_x). The non-linearities in the chemistry enhance the plume area-averaged ozone production.

Table 3.1: Influence of diffusion parameters on in-plume chemistry

Diffusion coefficients [m^2/s]	Remaining NO_x [%]	O_3 perturbation [kg/km]
$D_h = 05$, $D_v = 0.05$	88.23	0.06328
$D_h = 10$, $D_v = 0.10$	86.22	0.1695
$D_h = 15$, $D_v = 0.15$	84.92	0.2620
$D_h = 20$, $D_v = 0.20$	84.03	0.3391
$D_h = 25$, $D_v = 0.25$	83.35	0.4076
Box Model:	79.12	1.2581

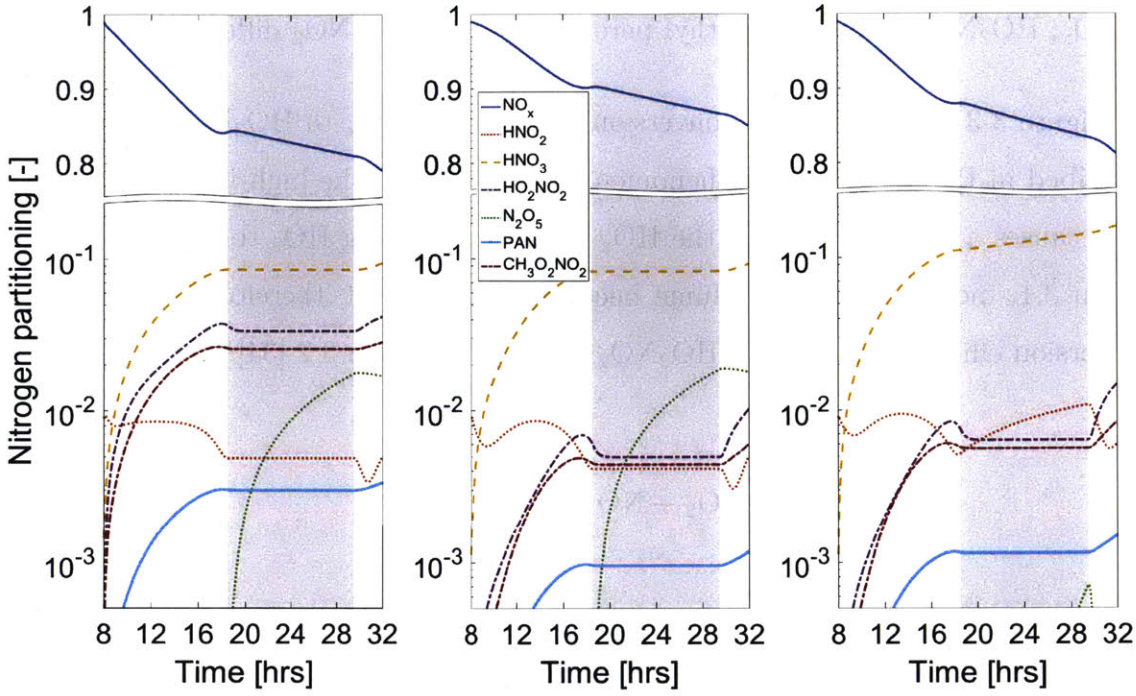

Figure 3-3: Partitioning of emitted nitrogen species as computed according to the single box model (left), the plume model in an ice sub-saturated environment (middle) and in an ice super-saturated environment (right). Shaded regions represent nighttime.

The partitioning of emitted NO_x is shown in Figure 3-3 as a function of plume time for the two models. Results in an ice super-saturated environment are also considered. All simulations are initialized with 1.5% of emitted NO_x being released as HNO_2 to account for the initial conversion in the core stream of the engine and the initial highly-turbulent phase [22]. The partitioning of all nitrogen species is pertinent to heterogeneous chemistry and particle micro-physics. As the plume diffuses out and undergoes chemical reactions, short-lived nitrogen oxides are converted to nitrogen reservoir species NO_z at a rate that depends on chemical background conditions, the local solar zenith angle and diffusion parameters.

The results presented in Figure 3-3 agree with other layered plume models in the literature [5, 23]. For the ice sub-saturated case, HNO_2 and nighttime N_2O_5 match with good precision between the box and the plume models. However, mixing ratios

of NO_x, HO_2NO_2, PAN and methyl peroxy nitrate $CH_3O_2NO_2$ differ.

Figure 3-3 shows that the conversion efficiency of NO_x to HO_2NO_2 is lower. As described in Petry et al., this phenomena arises because the high initial NO mixing ratio causes a repartitioning of the HO_x family, converting HO_2 to OH through Reaction 3.1, meaning that the plume becomes HO_2-limited, therefore decreasing the conversion efficiency of NO_2 to HO_2NO_2 through Reaction 3.2 [34].

$$HO_2 + NO \rightarrow NO_2 + OH \tag{3.1}$$

$$NO_2 + HO_2 \xrightarrow{M} HO_2NO_2 \tag{3.2}$$

The main chemical pathway of $CH_3O_2NO_2$ production is through the reaction of NO_2 with the methylperoxy radical (CH_3O_2). The only loss pathways of $CH_3O_2NO_2$ (and PAN) considered in the chemical mechanism are through unimolecular dissociations. Despite the high NO_2 mixing ratio (originating from NO titration) leading to higher PAN and $CH_3O_2NO_2$ mixing ratio in the innermost rings, the plume model predicts a lower estimate of PAN and $CH_3O_2NO_2$ perturbations. This is due to a lower concentration of NO_2 in the outer rings compared to the one of the box model, yielding a lower area-averaged production rate of $CH_3O_2NO_2$ (Equation 3.3), as depicted in Figure 3-4.

$$\begin{aligned}\overline{\left(\frac{d[CH_3O_2NO_2]}{dt}\right)}_{\text{prod}} &= \frac{k(T)}{A_p}\int\int [NO_2][CH_3O_2]dA \ \ldots \\ &= k(T)\overline{[NO_2][CH_3O_2]}\end{aligned} \tag{3.3}$$

where $\bar{\cdot}$ represents a plume averaged quantity. The same reasoning applies to PAN by considering peroxyacetyl radical (CH_3CO_3) instead of CH_3O_2.

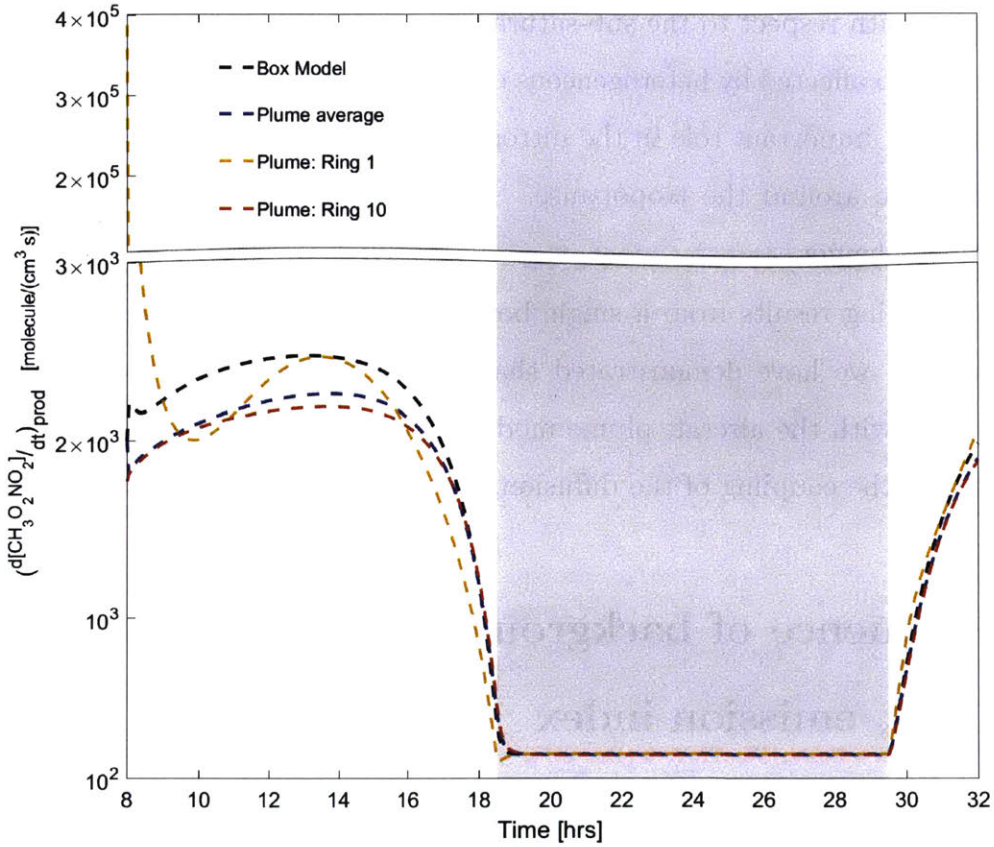

Figure 3-4: Production rate of methyl peroxy nitrate ($CH_3O_2NO_2$) as evaluated by the box (black dashed line) and the plume model.

The different results between the sub-saturated and super-saturated cases are consequences of heterogeneous chemical reactions on the surface of ice crystals, which have a larger aerosol surface area, compared to soot or sulfate aerosols. The differences between both simulations lie in the NO_x, HNO_3, HNO_2 and N_2O_5 mixing ratios, which are direct consequences of reactions 3.4 and 3.5:

$$NO_2 + \frac{1}{2}H_2O_{(l,\,s)} \xrightarrow{\text{Aerosol}} \frac{1}{2}HNO_3 + \frac{1}{2}HNO_2 \tag{3.4}$$

$$N_2O_5 + H_2O_{(l,\,s)} \xrightarrow{\text{Aerosol}} 2HNO_3 \tag{3.5}$$

In an environment with a high relative humidity, heterogeneous production of HNO_3 through N_2O_5 hydrolysis leads to an increase of roughly 90% in the nitric acid

partitioning with respect to the sub-saturated environment. The nighttime behavior of HNO_2 is also affected by heterogeneous depletion of NO_2. Halogen reservoir species do not play an important role in the nitrogen partitioning because of their relatively low abundance around the tropopause. Flying higher, in the stratosphere, could change this behavior.

By examining results from a single box model, where dilution is assumed to be instantaneous, we have demonstrated that using this method leads to conclusions that contrast with the aircraft plume model, whose ability to provide more accurate results lies in the coupling of the diffusion, chemical and micro-physical processes.

3.2 Influence of background NO_x mixing ratios and NO_x emission index

The presented results assess the photochemical conversion of emitted NO_x to reservoir species (NO_y) and ozone production over the course of the plume lifetime.

Plume-integrated $\Delta(NO_y)$ ($= \iint_A (NO_y - NO_y{}^a) dA$) is a conserved quantity throughout the plume lifetime and represents the total odd nitrogen emitted by the aircraft. Averaging the perturbation due to aircraft emissions allows us to study the time-dependent chemical conversions from one species to another. We can relate the perturbation of a species X to emitted NO_x and define an emission conversion factor as

$$\mathrm{ECF_X}(t) = \frac{\int \int_A ([\mathrm{X}](t) - [\mathrm{X}]^{\mathrm{a}}(t)) dA}{\int \int_A ([\mathrm{NO_y}](t) - [\mathrm{NO_y}]^{\mathrm{a}}(t)) dA}. \tag{3.6}$$

The emission conversion factor quantifies how many moles of species X are obtained for one mole of emitted NO_x, which is a function of time.

The in-plume ozone perturbation ($\Delta(O_3)(t)$) and the conversion efficiency of NO_x to NO_y are influenced in a non-linear manner by many parameters, such as the emission time and background conditions.

Simulations have been carried out to study the impact of the background chemical

composition for the plume-scale treatment and the box model.

Emission conversion factors have been computed and are shown in Figure 3-5. Both simulations have been integrated over 24 hours. For this study, the baseline case corresponds to a background NO_x mixing ratio of 100 ppt. The simulations started after a 5-day spin-up with the prescribed NO_x mixing ratio.

Figure 3-5 shows the area-integrated ozone perturbation 24 hours after emission as a function of the emission date for both models. The results agree qualitatively with the simulations from Petry et al. [34]. The single box model overestimates ozone production for any emission time, with emission conversion factors up to three times their respective values for the plume model. Discrepancies between the two models are greater during summertime where the absolute change in ECF_{O_3} is greater. The enhanced O_3 production rate is linked to the uniform NO_x-enriched environment and to a lower destruction through NO titration. Increasing background NO_x causes the ozone perturbation to decrease, even though the ozone in-plume mixing ratio is increased through the increase in that of the ambient air.

Another aspect is the correlation between the ozone emission conversion factor and the emission time. The ozone mixing ratio is driven by the photochemical equilibrium concentration of singlet oxygen O. Longer days increases the likelihood of molecular oxygen dissociation, and therefore, leads to higher ozone mixing ratio. The correlation appears in Figure 3-5.

The same simulation setup was used to obtain emission conversion factors as a function of date and emission time. Contours of O_3 and NO_x emission conversion factors are shown in Figure 3-6.

The O_3 emission conversion factor takes both positive, during local summer, and negative values, during wintertime, approximatively from November to February. It is also a function of emission time and peaks before sunset. This pattern is explained by a less efficient conversion of NO_x to reservoir species at night (as can be seen on Figure 3-3). The plume thus benefits from a larger nitrogen oxides mixing ratio at sunrise and leads to an enhanced daytime ozone production rate in this NO_x-rich environment. This explains why ECF_{NO_x} is lowest during summertime before sunset

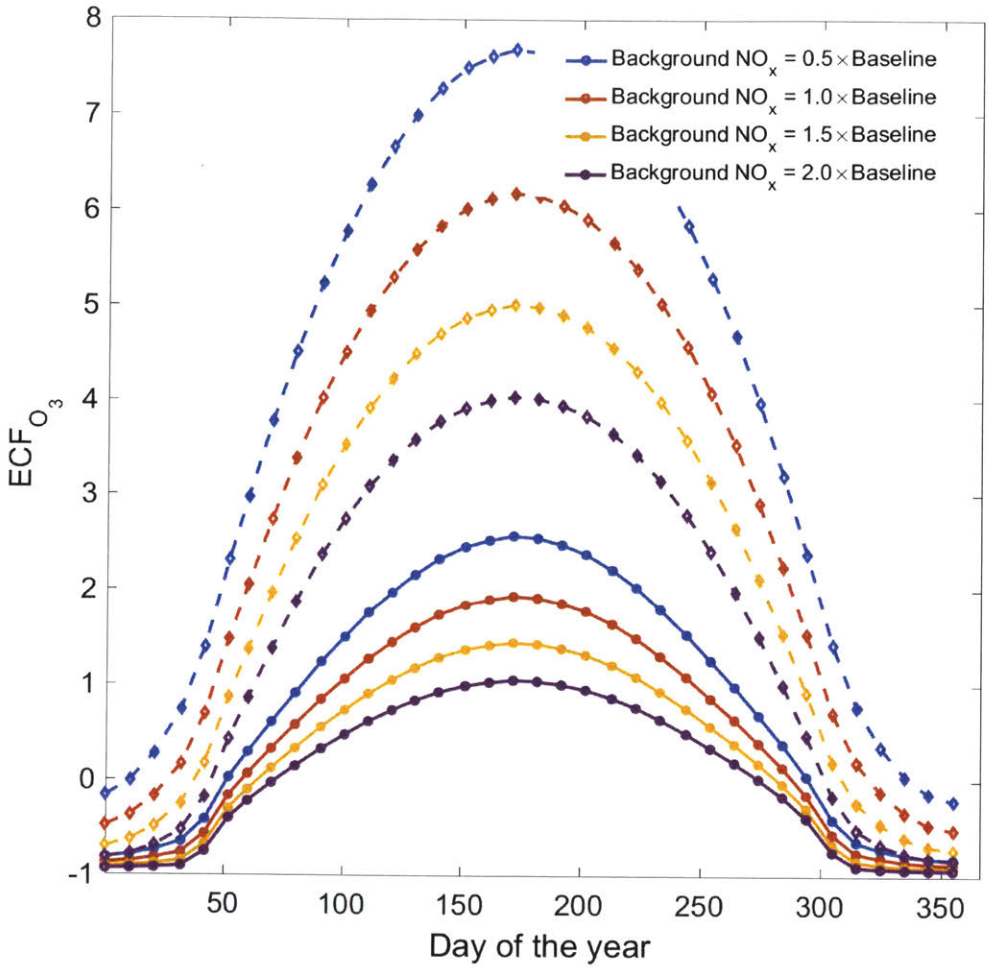

Figure 3-5: 24-hour ozone conversion factor from the emission of a B747-400 equipped with JT9D-7A engines at 08:00 AM local time for a single box model (dotted lines) and the plume model (continuous lines) as a function of day of the year. Different scenarios representing different background NO_x mixing ratios are displayed. The baseline case corresponds to a background NO_x mixing ratio of 100 ppt.

(for more details, see Appendix A). The absence of sunlight during winter leads to a uniform NO_x conversion factor with respect to emission time.

Figure 3-7 plots the dimensionless O_3 and NO_x ECF sensitivities to the nitrogen oxides emission index ($\frac{\partial ECF_X}{\partial EI_{NO_x}/EI^b_{NO_x}}$, where $EI^b_{NO_x}$ represents the baseline case and was set to 12 g/kg_{fuel}). The sensitivities have been computed with a third order accurate finite difference estimate.

Increasing the NO_x emission index causes the ozone perturbation per unit of emitted NO_x to decrease independently of the emission time and date. The area-

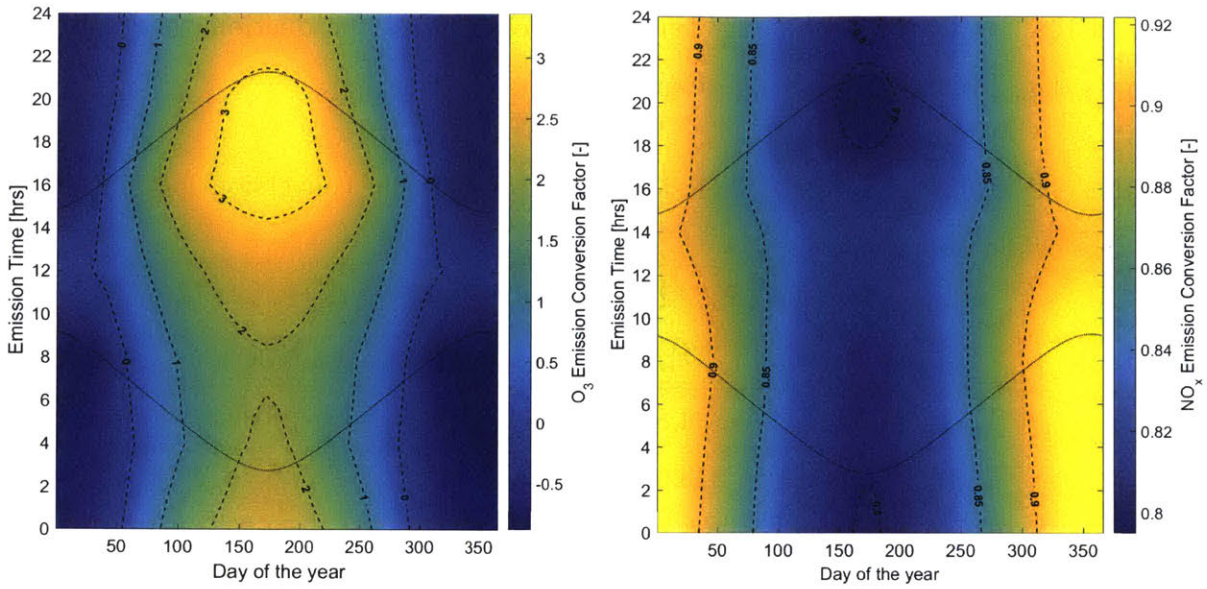

Figure 3-6: 24-hour O_3 (top) and NO_x (bottom) emission conversion factors from the emission of a B747-400 equipped with JT9D-7A engines at 60°N. Dotted lines represent sunrise and sunset at the given latitude. Background O_3 and NO_x mixing ratios were set to 52 ppb and 100 ppt respectively.

integrated ozone mixing ratio is enhanced as the emission index is increased. However, the perturbation per unit of NO_x emitted is subsequently decreasing (see Table 3.2). The sensitivity of ECF_{O_3} is directly proportional to the dimensionless quantity $\left(\frac{EI_{NO_x}}{\Delta[O_3]}\frac{\partial\Delta[O_3]}{\partial EI_{NO_x}} - 1\right)$, which is negative. A doubling of emitted NO_x results in less than a doubling in the in-plume ozone perturbation.

Table 3.2 describes some emission conversion factors and in-plume ozone perturbation for different values of emission index. The sensitivity study from Vohralik shows similar results [54]. A larger in-plume NO_x mixing ratio leads to a greater HO_2 depletion and therefore less HO_2NO_2 formation (according to Equations 3.1 and 3.2). The relative variations of $ECF_{HO_2NO_2}$ with respect to EI_{NO_x} are quite large. Similarly, conversion efficiencies of emitted NO_x to HNO_3, $CH_3O_2NO_2$ and PAN are negatively correlated to the emission index. On the other hand, the emission conversion factor of N_2O_5 is increased through nighttime chemistry.

It is also interesting to note that the integrated ozone perturbations $\Delta[O_3]$ are not monotonic functions of EI_{NO_x} (as depicted in Table 3.2). Ten hours after emissions,

the EI_{NO_x} = 20.0 g/kg_{fuel} case leads to a lower ozone production than EI_{NO_x} = 16.0 g/kg_{fuel} but is the highest after 24 hours.

Table 3.2: Influence of NO_x emission index on emission conversion factors and in-plume ozone perturbation

EI_{NO_x} [g/kg_{fuel}]	ECF_{O_3}(24 h) [%]	$\Delta[O_3]$ (10 h) [pptv]	$\Delta[O_3]$ (24 h) [pptv]
EI_{NO_x} = 8.0	324.8	45.07	59.33
EI_{NO_x} = 12.0	243.6	48.74	66.74
EI_{NO_x} = 16.0	191.0	49.23	69.79
EI_{NO_x} = 20.0	154.4	48.19	70.49
EI_{NO_x} [g/kg_{fuel}]	ECF_{NO_x} [%]	ECF_{HNO_3} [%]	$ECF_{HO_2NO_2}$ [%]
EI_{NO_x} = 8.0	77.15	16.05	23.25
EI_{NO_x} = 12.0	79.02	15.37	17.12
EI_{NO_x} = 16.0	80.53	14.61	13.09
EI_{NO_x} = 20.0	81.79	13.88	10.24
EI_{NO_x} [g/kg_{fuel}]	$ECF_{N_2O_5}$ [%]	$ECF_{CH_3O_2NO_2}$ [%]	ECF_{PAN} [%]
EI_{NO_x} = 8.0	0.8380	1.786	0.3017
EI_{NO_x} = 12.0	0.8534	1.259	0.2024
EI_{NO_x} = 16.0	0.8648	0.9321	0.1480
EI_{NO_x} = 20.0	0.8748	0.7104	0.1135

During the hemispherical winter, the absence of sunlight greatly limits the production of ozone and the conversion to nitrogen reservoir species, and thus, increasing the NO_x emission index enhances the plume area-averaged ozone but has very little effect on the perturbations per unit of NO_x emitted. Therefore, both sensitivities are small compared to their summertime values. Additionally, both metrics plotted in Figure 3-7 are weakly dependent on the emission time during local winter.

Local summer sees more variation, even if ECF_{O_3} and ECF_{NO_x} are more strongly dependent on emission day than emission time; the coefficient of variation (variance divided by the mean) of ECF_{NO_x} with respect to emission time is 3.86×10^{-5}, while it is 1.98×10^{-3} when taken with respect to emission date, approximately 50 times larger (the ratio is 11 when comparing ECF_{O_3}). The weak dependence on emission time is, as explained in Vohralik et al. [54], due to the fact that the same number of daylight hours is seen for each plumes at a given emission date (for an integration time of 24 hours). For different emission times, non-linearities in the chemical processes result only in small differences after 24 hours.

Figure 3-7 shows that increasing the NO_x emission index always results in a decrease in the ozone conversion efficiency. A higher NO_x emission index has little impact on either ECF_{NO_x} or ECF_{O_3} during wintertime since most of the emitted nitrogen is converted to reservoir species through the slow nighttime pathway (through NO_3 and N_2O_5) and ozone production rates are approximately 0 due to the absence of photons. The greatest decrease on the ozone conversion efficiency occurs at night during hemispherical summer.

As can be seen on Figure 3-1 or 3-3, NO_x conversion occurs faster during daytime (through reactions with OH and HO_2) and is more efficient if spatial gradients are small (a highly-concentrated small plume has a lower area-integrated chemical rate than a low-concentrated large plume, see Appendix A), therefore the remaining NO_x fraction will be lower if emissions occur around sunset or during nighttime. However, the sensitivity is the largest during summertime a few hours after sunrise, as seen on Figure 3-7. This is explained by the fact that increasing the NO_x emission index speeds up the conversion rate to NO_z, but the conversion occurs less effectively per unit of emission since the plume is small and highly-concentrated.

The presented results assess the photochemical conversions of NO_x emissions in aircraft wakes and their dependency on the engine emission index and background NO_x mixing ratios. They are in agreement with findings from the literature [26, 34, 54]). This section showed that a plume-scale treatment of chemical processes reduced ozone conversion efficiencies by up to three times compared to a single-box model

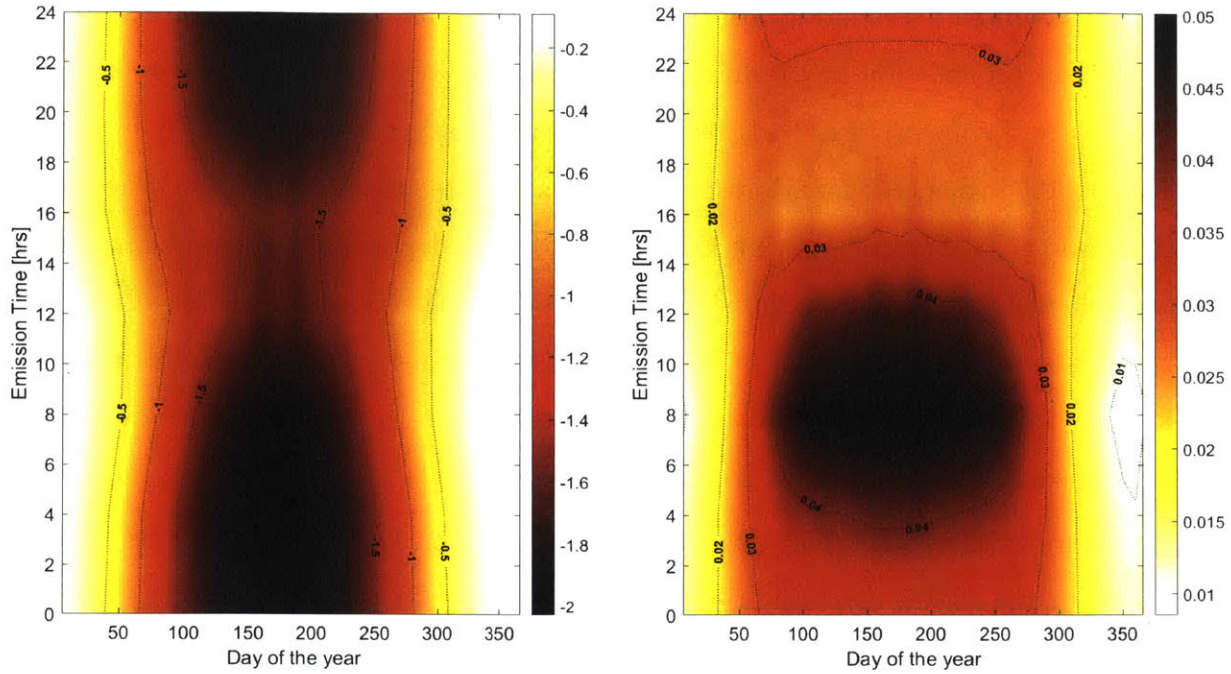

Figure 3-7: O_3 (left) and NO_x (right) emission conversion factor sensitivities as a function of local time and day of the year at the time of emission.

and slowed conversion of nitrogen oxides to reservoir species and altered the nitrogen partitioning. Time dependencies of emission conversion factors and sensitivities to engine emission index have been obtained.

3.3 Influence of flight location

The pressure and latitude dependence of the local influence of aircraft emission was quantified. The considered pressure and latitude ranges extend from 750 hPa to 150 hPa and from 0°N to 90°N. Temperature data was taken from monthly-averaged MERRA2 meteorological data, for the year 2013. To capture the spatial variations of a single flight's emission conversion factors, background conditions and photolysis rates were taken from GEOS-Chem. To also consider seasonal effects, simulations have been carried out for emissions taking place on the winter and summer solstices as well as during the spring equinox, on March 21st.

Simulations using both models have been carried out. Results are presented in

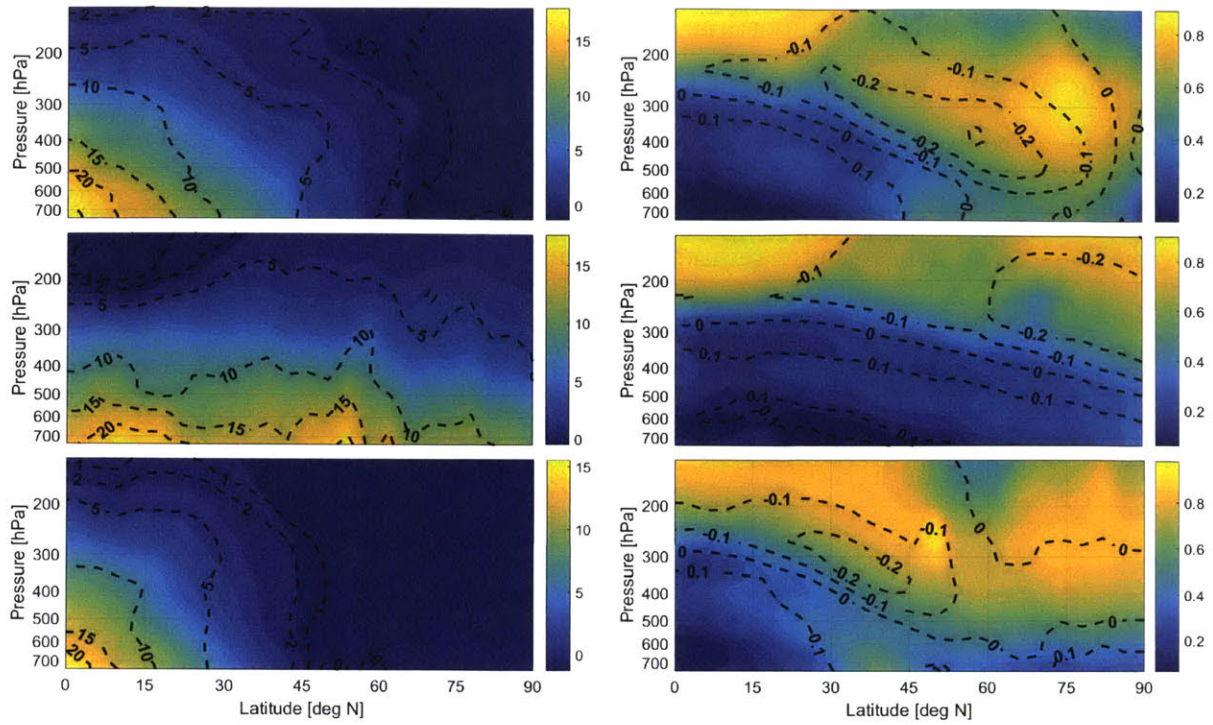

Figure 3-8: Contour plots of O_3 (left) and NO_x (right) conversion emission factor as a function of latitude and pressure, 24 hours after emission. The isolines represent the difference between the single box model and the aircraft plume model. Simulations were carried out for emissions at 8:00AM on March 21st, June 21st and December 21st (from top to bottom).

Figure 3-8 in terms of O_3 and NO_x emission conversion factors. Isolines of absolute errors between the single box model and the aircraft plume model are also plotted for both species.

The results point to a clear link between ozone production efficiency and latitude and pressure. Increasing pressure enhances the ozone emission conversion for the same amount of emitted NO_x, in regions with sufficient sunlight. The amount of sunlight drives ozone production, as little ozone is generated in the most northern latitudes during hemispherical winter. At high flight altitudes or in cold regions, the daytime NO_x-driven ozone production is of the order of magnitude of the ozone loss at dusk and the early titration effect, leading to a slightly positive or, sometimes negative, in-plume ozone perturbation as depicted in Vohralik et al. [54].

The box model overestimates the amount of produced ozone by up to 110%, and

performs worst during summertime as ozone production is enhanced.

The NO_x emission conversion factor, also displayed in Figure 3-8, is correlated to ambient temperature (a temperature increase speeds the conversion to reservoir species) and shows little dependence on the actual amount of sunlight and on seasonal variations. The atmospheric temperature lapse rate being typically negative in the troposphere, the conversion of NO_x to NO_y decreases with altitude, going from an average value of 0.3 at 700 hPa to approximately 0.75 at 150 hPa. Highest conversion occurs in hotter air, around the equator and the tropics.

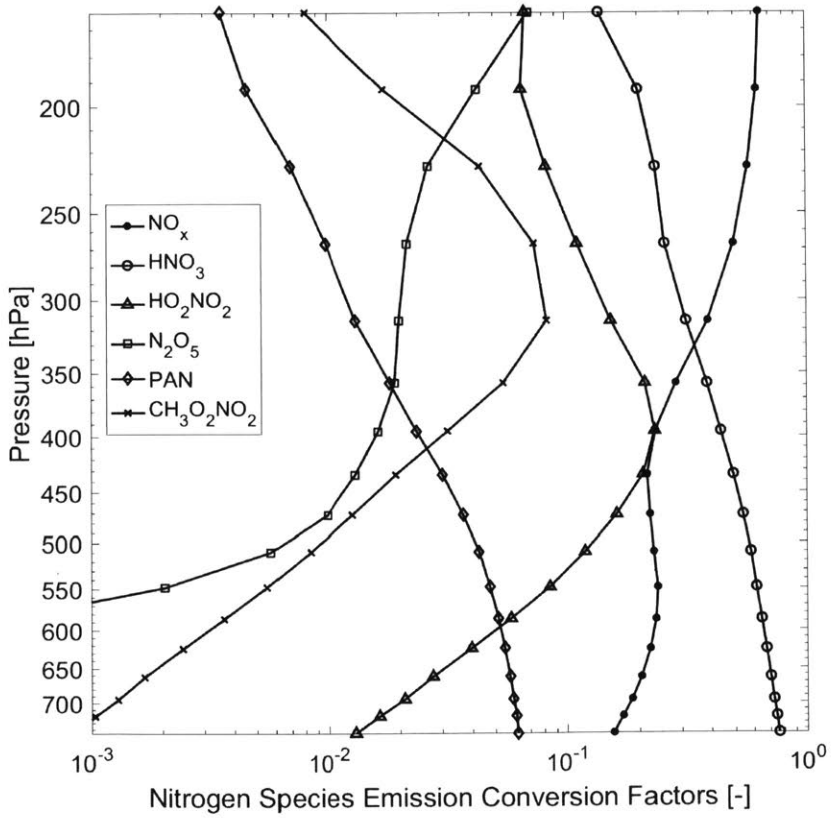

Figure 3-9: Altitude dependency of the 24-hour emission conversion factors of the main nitrogen species at 60°N at the summer solstice.

Figure 3-9 depicts the different nitrogen species emission conversion factors, at 60°N on June 21st, plotted as a function of pressure. HNO_3 and HO_2NO_2 are the main reservoir species in the pressure range considered. Conversion to nitric acid rises with pressure, reaching 76% at 750 hPa and 14% at 160 hPa.

Conversion to N_2O_5 increases importance with altitude, as lower temperatures reduce the thermal decomposition to NO_2 and NO_3. PAN production is maximized at higher pressures. Conversion to $CH_3O_2NO_2$ peaks around 300 hPa and becomes negligible outside of the 160 hPa - 500 hPa pressure range because higher temperatures and pressures enhance $CH_3O_2NO_2$ thermal breakdown and decrease its lifetime.

Production of O_3 and conversion from NO_x to NO_y was estimated as a function of pressure, latitude and including seasonal effects. While the remaining fraction of NO_x is mainly affected by temperature, the O_3 emission conversion factor is influenced by many parameters, such as solar zenith angle, temperature but also background NO_x.

3.4 Influence of overlapping flights

This section aims at describing the potential impact of plume overlapping on in-plume chemistry, as in a flight corridor, by considering a maximum of six flights, at 2-hour intervals.

Figure 3-10 shows the impact on successive flight emissions and plume overlapping on O_3, sulfate aerosol surface area, N_2O_5 and HNO_3 perturbations for emissions at 8:00 PM local time. Results from the simulations show that emissions from a given flight reduce the integrated ozone production caused by earlier flights. The magnitude of the perturbation, 24 hours after the first flight, greatly depends on flight history and is balanced by early ozone destruction and long-time ozone production. In their work, Cameron et al. found that the decrease in the ozone perturbation from additional flights was not sufficient to overcome ozone production from previous flights, leading to a positive in-plume ozone perturbation [5]. Table 3.3 shows potential situations where ozone production from older flights cannot be overcome by recently released emissions. Here, we show that it is possible to find scenarios where the overall ozone contribution is negative.

Emissions at nighttime reduce the ozone perturbation through early NO titration. On the other hand, daytime ozone production processes are positively correlated to the NO_x concentrations. Additional flights increase the strength of both mechanisms.

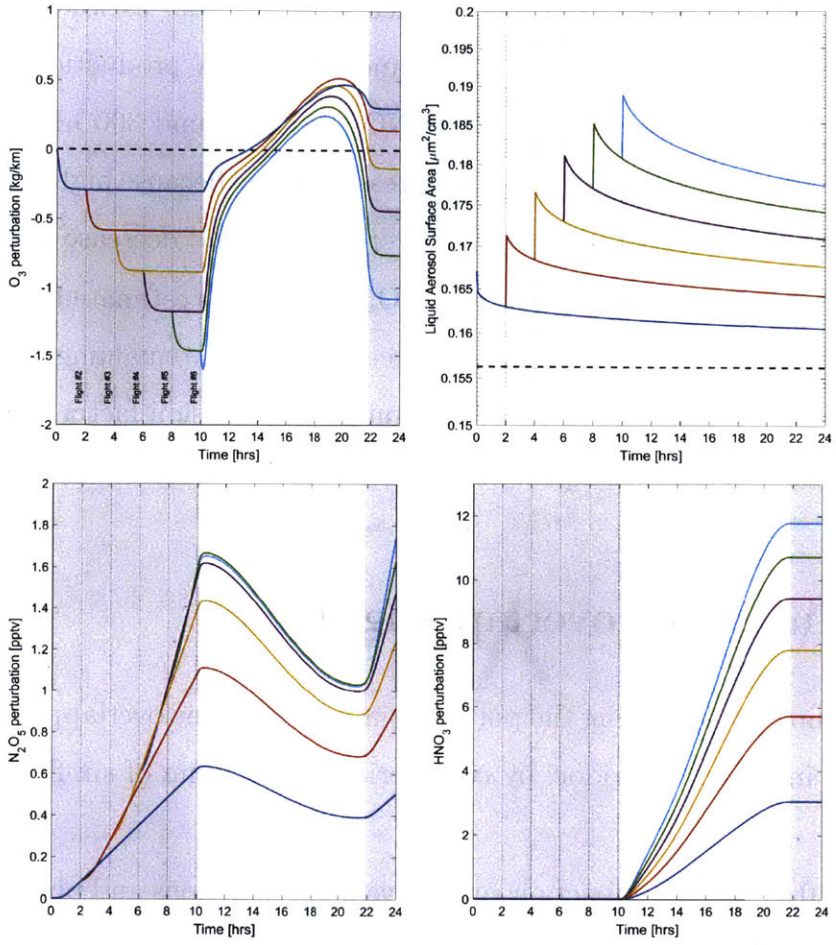

Figure 3-10: Time evolution of in-plume O_3 (top left), liquid aerosol surface area (top right), N_2O_5 (bottom left) and HNO_3 (bottom right) perturbations for a successive number of flight, with a time interval of 2 hours. Each vertical dotted line represents a flight instance. On the second graph, the black dashed line represents the background liquid aerosol surface area. The shaded areas depicts nighttime conditions.

On Figure 3-10, it can be seen that this a non-linear effect. For instance, two consecutive flights lead to a greater ozone perturbation 20 hours after emissions compared to a single or three consecutive flights. However, the 24-hour ozone perturbation is a decreasing function of the number of flights in this case, as shown in Table 3.3. Additional flights increase the liquid aerosol number density, which is then reduced through volume-conserving coagulation phenomena. Heterogeneous chemistry, as well as daytime and nighttime chemistry, affect the evolution of the main nitrogen reservoir species.

The daytime NO_x conversion pathway is mainly described by the following reactions 3.7 and 3.8. NO_2 reacts with HO_x to produce HNO_3 and HO_2NO_2:

$$NO_2 + OH \xrightarrow{M} HNO_3 \tag{3.7}$$

$$NO_2 + HO_2 \xrightarrow{M} HO_2NO_2 \tag{3.8}$$

Nighttime conversion of NO_x to reservoir species happen mainly through reactions 3.9 through 3.11 and is dominated by conversion to N_2O_5 and eventually to nitric acid HNO_3, at a rate that depends on the aerosol distribution profile:

$$NO_2 + O_3 \rightarrow NO_3 + O_2 \tag{3.9}$$

$$NO_3 + NO_2 \xrightarrow{M} N_2O_5 \tag{3.10}$$

$$N_2O_5 + H_2O_{(l,s)} \xrightarrow{\text{Aerosol}} 2HNO_3 \tag{3.11}$$

Nitric acid production therefore occurs through conversion of NO_2 during daytime and by N_2O_5 hydrolysis on the aerosol surface at night. As it appears on Figure 3-10, no HNO_3 production is observed at night, and thus, the effect of heterogeneous chemistry is limited, as the total aerosol surface area, dominated in this case by liquid aerosols, remains quite small, despite cumulative emissions.

Simulations of a single flight with a varying fuel sulfur content (FSC) showed no effect on gas-phase chemistry. The contribution of sulfate aerosols to heterogeneous chemistry is more largely dependent on the background size distribution [54], since emitted aerosols remain small even after a few hours after their formation.

Multiple overlapping flights affect the background chemical environment in a non-linear manner. Cumulative flights reduce the 24-hour ozone perturbation, and this decrease can be sufficient to overcome ozone production from earlier flights and yield a negative contribution. The total contribution is highly dependent on the date and

Table 3.3: Influence of emissions from successive flights on ozone perturbation. Values are estimated 24 hours after emission for an emission time of 8:00 AM for March 16th, June 16th and December 16th. A total of 6 flights have been simulated with a two hour interval.

Date	Δ [O_3] ([g/km])					
Flight #	1	2	3	4	5	6
March 16	142	42	-51	-137	-222	-304
June 16	601	571	507	454	409	365
Dec. 16	-277	-577	-877	-1176	-1473	-1770

time of emission as well as the flight schedule.

3.5 Contrail micro-physical and chemical properties

In the following, the results describe the micro-physical and chemical properties of a flight that formed a condensation trail.

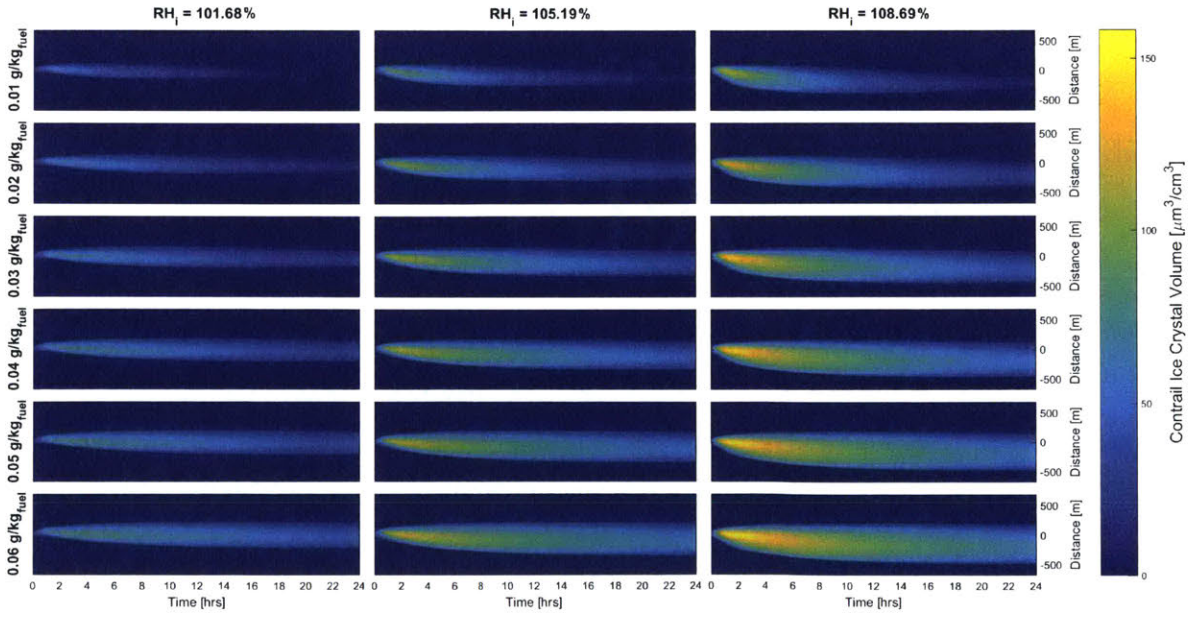

Figure 3-11: Contrail ice crystal volume density averaged across the horizontal direction for different relative humidities with respect to ice and for different soot emission indices. The graphs share the same color scale. The cruising altitude of the contrail-generating aircraft is at $z = 0$.

The results are presented as a function of background relative humidity and the aircraft soot emission index. A soot radius of 40 nm was used in our simulations. To limit the number of variables and to qualitatively assess how certain metrics vary with parameters, such as emission indices and background relative humidity, no synoptic scale updraft nor mesoscale vertical air motions have been considered in the following simulations. However, it is clear that the cooling or heating related to these wind patterns has a non-negligible effect on contrail-cirrus evolution.

Figure 3-11 shows contours of horizontally-averaged ice crystal volume. This indicates that the contrail lifetime varies and can be greater than 10 hours in agreement with observations [14,29]. Contrails consist of a core region where the relative humidity is close to 100% (because the mixing of supersaturated air happens on a timescale much greater than the timescale required for the ice crystals to grow) and an outer region, forming a fall-streak. Both of these have different micro-physical properties. The core consists of a large number density of ice crystals with a relatively low ice mass while the edge of the contrail has a low number density but uptakes a large part of the surrounding water vapor, leading to a spatially non-uniform contrail ice mass. This agrees with results from Unterstrasser et al. [49].

The simulations were set up with a uniform initial relative humidity with respect to water and assuming a constant temperature lapse rate. The depth of the moist layer is therefore directly linked to the background supersaturation. As seen in Figure 3-11, higher background relative humidities increase the total contrail ice crystal volume due to a larger depth of the supersaturated region, in which the contrail fully expands from approximatively the flight altitude down to the location of the supersaturation altitude ($RH_i = 1$). The contrail properties depend on the vertical profile of the relative humidity. Setting the updraft velocity to zero decreases the average ice crystal radius and settling velocity, and therefore is most likely to increase the contrail lifetime. The lifetimes observed here are thus upper bounds.

Ambient meteorological data controls the initial ice mass which results in a change in ice crystal sizes for different soot emission index, varying from $2 \times 10^{13} - 1.2 \times 10^{14}$ $/\mathrm{kg_{fuel}}$. We first consider a case where the soot emission index is greater than the

baseline case. An enhanced soot emission index means that ice crystals are initially smaller on average but results in a larger ice mass in the long term. As explained in Unterstrasser et al. [50], a higher ice crystal number density leads to a quicker uptake of water vapor from ambient air and increases the outward diffusion flux. Additionally, since the settling velocities are increasing with crystal radius, the downward flux of particles out of the contrail region decreases for a larger emission index and the contrail lifetime as well as the contrail ice mass are, therefore, increased.

The expansion of the fall-streak dehydrates the core of the contrail. As the particles fall to a sub-saturated region, they release their ice mass and this process contributes to the dehydration of the UTLS. This dehydration occurs all across the depth of the supersaturated layer.

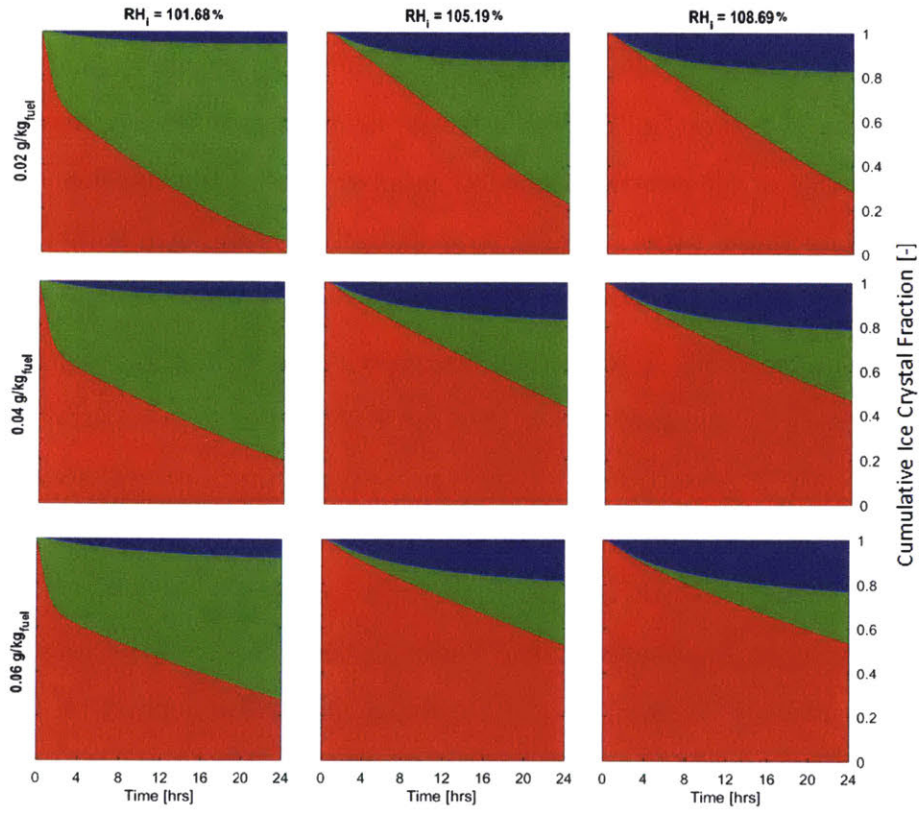

Figure 3-12: Ice crystal number loss in contrails. The red area shows the fraction of existing ice crystals, the green area the fraction lost due to sedimentation and the blue area the fraction lost to aggregation processes. The graphs are normalized by the initial number of ice crystal.

Contrail ice crystals are lost by two pathways and their number is controlled by

environmental factors as well as aircraft and fuel parameters. Figure 3-12 depicts the fraction of the initial ice crystal number lost to aggregation (in blue) and by sedimentation (in green). The remaining fraction is plotted in red. Loss processes are heavily correlated to ambient conditions and their fluctuations in time and space. The results show that losses through sedimentation are dominant at low relative humidities and low soot numbers while, for other conditions, losses through both mechanisms have a similar share.

At barely super-saturated conditions, ice crystals are lost to sedimentation on the timescale of a few hours while they last for approximatively more than 15 hours in a very humid environment. At the lowest relative humidity studied here (RH_i = 101.68%), a contrail formed at the edge of the supersaturation line and therefore losses through sedimentation occur on a short timescale. Aggregation losses gain greater importance at higher relative humidities. Larger ice crystals increase the likelihood of a coagulation event occurring. Additionally, for a given lapse rate, a larger supersaturation increases the depth of the moist layer and therefore reduces the sedimentation flux of particles since the supersaturation surface is located further away from the initial formation altitude.

A larger soot emission index reduces the loss through sedimentation and enhances the aggregation loss. This is due to the presence of smaller crystals that fall slower and persist longer, reducing the downward particle flux and allowing for more losses through coagulation processes.

Throughout its lifetime, a contrail sees a change in its micro-physical properties. Figure 3-13 shows a contour of probability density functions of crystal number, area and volume integrated over the contrail's cross-section. A second mode appears a few minutes after the contrail formation while the initial mode is relatively stable and does not grow with time. This bimodal distribution corresponds to the core region and the fall-streak. The fall-streak takes up a large amount of water vapor while having a low number of ice crystals. The location of this second peak is set by the background relative humidity and the depth of the supersaturated layer. A similar pattern has been observed by Unterstrasser et al. as soon as 30 minutes after

initial formation [51]. Even if the number of particles in the outer region is low, their contribution to the cross-sectional area is greater which could have important consequences for the assessment of contrails' radiative forcing.

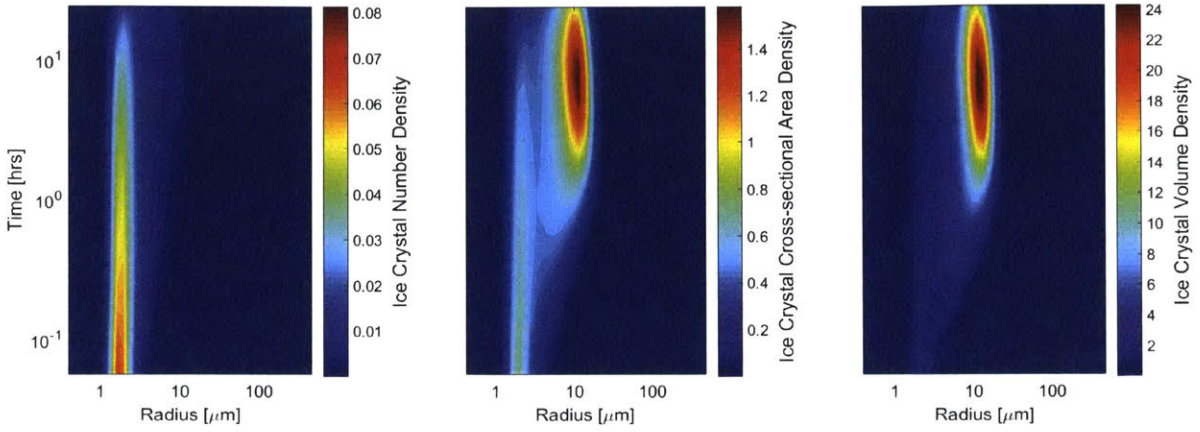

Figure 3-13: Contours of number (left), cross-sectional area (middle) and volume (right) probability densities as a function of time. The integrated PDFs are in $\#/cm^3$, $\mu m^2/cm^3$ and $\mu m^3/cm^3$ respectively.

Figure 3-14 highlights the evolution of some chemical species over the contrail lifetime. Perturbations of O_3 and N_2O_5 as well as the total (gaseous + solid) water mixing ratio are displayed. Asymmetry in the vertical profiles arises because of heterogeneous chemistry on the ice crystal surface and micro-physical processes.

Ozone titration effects from initial NO conversion are visible in the first few minutes of the plume which are then overcome by daytime ozone production in a NO_x-rich environment. Ozone sees no effect from heterogeneous chemistry. Sunset occurs at a plume time of 10 hours, therefore explaining why the ozone profiles at 12 and 18 hours spreads outwards without observing chemical production.

The asymmetry in the dinitrogen pentoxide (N_2O_5) profile arises from nighttime production and hydrolysis on the surface of aerosols to form HNO_3. The large surface area in the core and lower side of the plume leads to a higher conversion of N_2O_5 to HNO_3. NO_3 is also affected by heterogeneous chemistry in the lower plume and its higher nighttime mixing ratio in the upper plume leads to a positive N_2O_5 perturbation after sunrise.

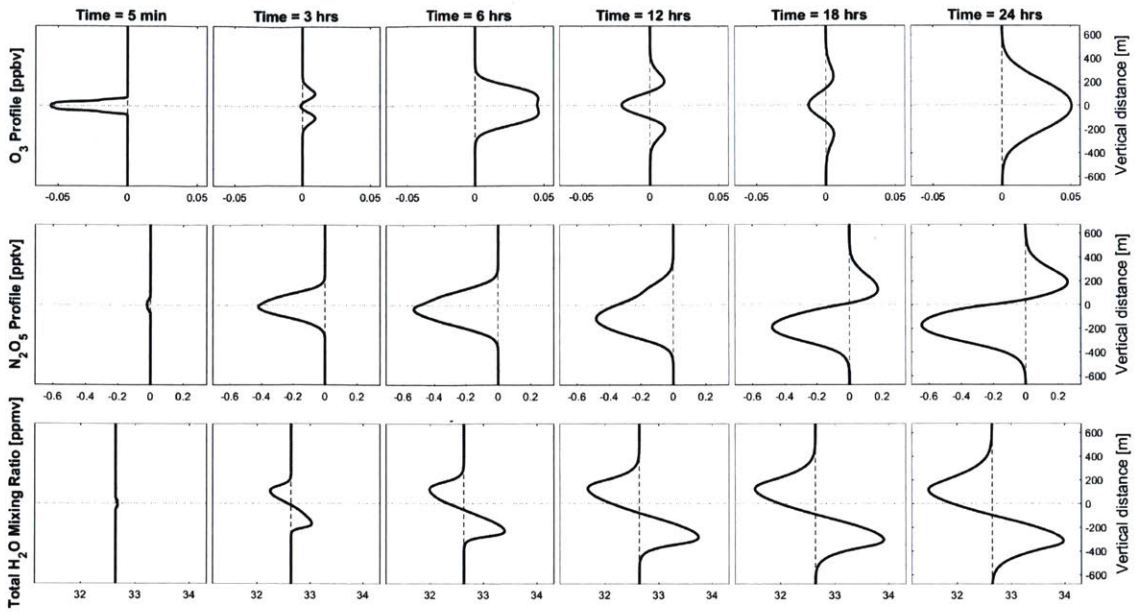

Figure 3-14: Profiles of O_3 (top), N_2O_5 (middle) perturbations as well as total water (gaseous and solid phase) mixing ratio (bottom) at different times. Times showed at the top represent time after emission. Emission took place at 8:00 AM local time. Sunrise and sunset occurred at 6:00 AM and 6:00 PM local time. The cruising altitude of the contrail-generating aircraft is at $z = 0$. Units are in ppbv, pptv and ppmv respectively.

Not displayed here is the quantity $NO_z - HNO_3 = NO_y - NO_x - HNO_3$. The latter peaks in the upper part of the plume and has a minimum around -300 m. The reservoir species NO_z mixing ratio increases uniformly over time but is faster in the lower plume owing to conversion from NO_2 to HNO_3 and HNO_2 through on-aerosol reaction. NO_z has its maximum at -15 m.

A higher aerosol surface area enhances N_2O_5 depletion and conversion to HNO_3. This can be seen on the area-integrated mixing ratios in Figure 3-3 when comparing a contrail producing flight to the case where no contrail is formed.

The water mixing ratio is affected by ice crystal micro-physics. Nuclei in the moist layer take up gaseous water up to saturation, which is then displaced to lower altitudes, dehydrating the cruising altitude.

The results from this section show that contrail micro-physics and chemical composition are affected by many meteorological as well as aircraft-dependent parameters. Among the meteorological parameters, the evolution of a contrail-cirrus is affected

by the local relative humidity profile [49]. All cases studied showed the same contrail pattern, composed of a core saturated region, whose crystal size is approximately time-independent, and a peripheral region composed of larger crystals. The latter's crystal size is dependent on the ambient relative humidity.

The evolution of a contrail has also been found to depend on the number of nuclei emitted. A larger soot emission index reduces the diameter on average and decreases the settling velocity, making the contrail last longer. Additionally, the soot emission number has an impact on the optical properties all along the contrail lifetime. As described by Unterstrasser et al., reducing the soot emission number could lower the contrail-cirrus radiative forcing [50].

Chemical species have an asymmetric profile across the contrail width. A greater aerosol surface area in the lower side of the plume leads to larger chemical rates through heterogeneous chemistry. The extent of the asymmetry depends on ice crystal micro-physical parameters and therefore on meteorological data as well as aircraft parameters.

Chapter 4

Conclusions

A fully parameterized aircraft plume has been developed to estimate local perturbations of species mixing ratios in an aircraft wake. Regional and global-scale models base their global assessment on engine exit emission indices. The results from this paper confirm that neglecting the non-linear plume-scale processes lead to inaccuracies in the assessment of O_3 perturbations and of the conversion of NO_x ($= NO + NO_2$) to reservoir species. Enhanced diffusion parameters reduce but do not eliminate errors associated with single-box models.

A parametric study showed that the 24 hour ozone emission conversion factor is greater before sunset during local summer. Sensitivities of the in-plume ozone perturbation to aircraft and fuel parameters have been estimated. Even though the in-plume O_3 mixing ratio increased due to increased NO_x emission indices, the ozone emission conversion factor decreased. This reduction is a function of date and emission time and is lower during local winter.

Conversion factors have also been found to be strongly dependent on the seasonality, as well as meteorological data. Daytime duration, temperature and different NO_x background concentrations, at different latitudes, have been found to influence in-plume ozone production.

Overlapping flights have the potential to change the local chemical perturbation. Even if the problem is non-linear and having more flights can increase daytime ozone, we found that the 24-hour area-integrated ozone perturbation decreases as more flights

are added.

Ice crystal micro-physics has been coupled with plume processes. The results show that an enhanced soot emission index increases the contrail lifetime and the horizontally-integrated aerosol cross-sectional area. Additionally, a higher nuclei number density was found to reduce the loss through sedimentation by reducing the average crystal radius.

A contrail is composed of two regions, a nuclei-rich region at the core of the contrail whose crystal size mode is time-independent and a moist region at the periphery where crystals grow in size. The latter appears shortly after the initial formation of the contrail.

Profiles of chemical species have been obtained and showed non-uniformities in the vertical direction due to gradients in the aerosol surface area. Some species, such as O_3, are unaffected at the pressure and temperature considered.

Looking at the results above, it is recommended that atmospheric models include a plume-scale treatment of aircraft emissions in the form of a look-up table. Parameters could include meteorological data (temperature, pressure, humidity, Brunt-Väisäla frequency), chemical data (O_3, NO_x background mixing ratios), flight properties (longitude, latitude, date and emission time) as well as engine and fuel characteristics (emission indices, fuel properties).

Appendix A

Plume-averaged NO_X chemical rate

We assume that the conversion of NO_x to reservoir species is dictated by the daytime conversion pathway through the following reactions:

$$NO_2 + OH \xrightarrow{M} HNO_3 \tag{A.1}$$

$$NO_2 + HO_2 \xrightarrow{M} HO_2NO_2 \tag{A.2}$$

The chemical reaction rate can be written as:

$$\frac{d[NO_2]}{dt} = -(k_1[OH] + k_2[HO_2])[NO_2]$$
$$\frac{d[NO_2]}{dt} = -k_{eff}[HO_x][NO_2]$$

where HO_x has been defined such that $[HO_x] = \frac{k_1[OH]+k_2[HO_2]}{k_1+k_2}$.

We assume that the concentration field at a fixed point can be expressed as the sum of spatially-averaged quantity and the instantaneous fluctuation, such that:

$$[NO_2] = \overline{[NO_2]} + [NO_2]'$$
$$[HO_x] = \overline{[HO_x]} + [HO_x]'$$

The chemical conversion rate of NO_x can therefore be written as:

$$\begin{aligned}\frac{d\overline{[NO_2]}}{dt} &= -k_{\text{eff}} \times \overline{[HO_x][NO_2]} \\ &= -k_{\text{eff}} \times \left(\overline{[HO_x]} \times \overline{[NO_2]} + \overline{[HO_x]' \times [NO_2]'}\right)\end{aligned}$$

The first term on the right hand side leads to a net depletion. NO_2 is an emitted species. Therefore, the NO_2 concentration is positive in the core of the plume, while it is negative far away. HO_x, however, gets depleted to form HNO_3 and HO_2NO_2. Therefore, $[HO_x]' \leq 0$ in the inner plume and $[HO_x]' \geq 0$ outside of the core. Thus, the second term reduces NO_x conversion and is proportional to the correlation of the fluctuations. If both fluctuations are negatively correlated, the depletion is reduced compared the case where the fields are uniform.

This explains why, for the same emission quantity, a small plume with large spatial fluctuations leads to a lower conversion compared to a large plume with smaller gradients.

Bibliography

[1] H Appleman. The formation of exhaust condensation trails by jet aircraft. *Bull. Amer. Meteorol. Soc.*, 34:14–20, 1953.

[2] Kenneth V Beard and Harry T Ochs III. Collisions between small precipitation drops. part ii: Formulas for coalescence, temporary coalescence, and satellites. *Journal of the Atmospheric Sciences*, 52(22):3977–3996, 1995.

[3] GP Brasseur, RA Cox, D Hauglustaine, I Isaksen, J Lelieveld, DH Lister, R Sausen, U Schumann, A Wahner, and P Wiesen. European scientific assessment of the atmospheric effects of aircraft emissions. *Atmospheric Environment*, 32(13):2329–2418, 1998.

[4] Guy P Brasseur, Jean-François Müller, and Claire Granier. Atmospheric impact of nox emissions by subsonic aircraft: A three-dimensional model study. *Journal of Geophysical Research: Atmospheres*, 101(D1):1423–1428, 1996.

[5] Mary A Cameron, Mark Z Jacobson, Alexander D Naiman, and Sanjiva K Lele. Effects of plume-scale versus grid-scale treatment of aircraft exhaust photochemistry. *Geophysical Research Letters*, 40(21):5815–5820, 2013.

[6] D Cariolle, D Caro, R Paoli, DA Hauglustaine, B Cuenot, A Cozic, and R Paugam. Parameterization of plume chemistry into large-scale atmospheric models: Application to aircraft nox emissions. *Journal of Geophysical Research: Atmospheres*, 114(D19), 2009.

[7] Valeriu Damian, Adrian Sandu, Mirela Damian, Florian Potra, and Gregory R Carmichael. The kinetic preprocessor kpp-a software environment for solving chemical kinetics. *Computers & Chemical Engineering*, 26(11):1567–1579, 2002.

[8] Tilman Dürbeck and Thomas Gerz. Dispersion of aircraft exhausts in the free atmosphere. *Journal of Geophysical Research: Atmospheres*, 101(D20):26007–26015, 1996.

[9] Sebastian D Eastham, Debra K Weisenstein, and Steven RH Barrett. Development and evaluation of the unified tropospheric–stratospheric chemistry extension (UCX) for the global chemistry-transport model GEOS-Chem. *Atmospheric Environment*, 89:52–63, 2014.

[10] Veronika Eyring, David S Stevenson, Axel Lauer, Frank J Dentener, Tim Butler, William J Collins, Kirsten Ellingsen, Michael Gauss, Didier A Hauglustaine, Ivar SA Isaksen, et al. Multi-model simulations of the impact of international shipping on atmospheric chemistry and climate in 2000 and 2030. *Atmospheric Chemistry and Physics*, 7(3):757–780, 2007.

[11] NHJ Fletcher. Size effect in heterogeneous nucleation. *The Journal of Chemical Physics*, 29(3):572–576, 1958.

[12] Walton Forstall and Ascher H Shapiro. Momentum and mass transfer in coaxial gas jets. *Journal of Applied Mechanics-Transactions of the ASME*, 17(4):399–408, 1950.

[13] W Haag, B Kärcher, J Ström, A Minikin, U Lohmann, J Ovarlez, and A Stohl. Freezing thresholds and cirrus cloud formation mechanisms inferred from in situ measurements of relative humidity. *Atmospheric Chemistry and Physics*, 3(5):1791–1806, 2003.

[14] Hironobu Iwabuchi, Ping Yang, KN Liou, and Patrick Minnis. Physical and optical properties of persistent contrails: Climatology and interpretation. *Journal of Geophysical Research: Atmospheres*, 117(D6), 2012.

[15] Mark Z Jacobson, Richard P Turco, Eric J Jensen, and Owen B Toon. Modeling coagulation among particles of different composition and size. *Atmospheric Environment*, 28(7):1327–1338, 1994.

[16] MZ Jacobson. Numerical solution to drop coalescence/breakup with a volume-conserving, positive-definite, and unconditionally stable scheme. *Journal of the Atmospheric Sciences*, 68(2):334–346, 2011.

[17] A Jaecker-Voirol and Ph Mirabel. Heteromolecular nucleation in the sulfuric acid-water system. *Atmospheric Environment (1967)*, 23(9):2053–2057, 1989.

[18] Jae Gun Jung, Spyros N Pandis, and Peter J Adams. Evaluation of nucleation theories in a sulfur-rich environment. *Aerosol Science and Technology*, 42(7):495–504, 2008.

[19] B Kärcher. A trajectory box model for aircraft exhaust plumes. *Journal of Geophysical Research: Atmospheres*, 100(D9):18835–18844, 1995.

[20] B Kärcher, Th Peter, U Mi Biermann, and U Schumann. The initial composition of jet condensation trails. *Journal of the Atmospheric Sciences*, 53(21):3066–3083, 1996.

[21] Bernd Kärcher. Aviation-produced aerosols and contrails. *Surveys in Geophysics*, 20(2):113–167, 1999.

[22] Bernd Kärcher, R Busen, A Petzold, FP Schröder, U Schumann, and EJ Jensen. Physicochemistry of aircraft-generated liquid aerosols, soot, and ice particles: 2. comparison with observations and sensitivity studies. *Journal of Geophysical Research: Atmospheres*, 103(D14):17129–17147, 1998.

[23] Anne Gunn Kraabøl, Paul Konopka, Frode Stordal, and Hans Schlager. Modelling chemistry in aircraft plumes 1: comparison with observations and evaluation of a layered approach. *Atmospheric environment*, 34(23):3939–3950, 2000.

[24] David S Lee, David W Fahey, Piers M Forster, Peter J Newton, Ron CN Wit, Ling L Lim, Bethan Owen, and Robert Sausen. Aviation and global climate change in the 21st century. *Atmospheric Environment*, 43(22):3520–3537, 2009.

[25] Joosung J Lee, Stephen P Lukachko, Ian A Waitz, and Andreas Schafer. Historical and future trends in aircraft performance, cost, and emissions. *Annual Review of Energy and the Environment*, 26(1):167–200, 2001.

[26] Ernst Willem Meijer. *Modelling the impact of subsonic aviation on the composition of the atmosphere.* Technische Universiteit Eindhoven, 2001.

[27] EW Meijer, PFJ Van Velthoven, WMF Wauben, JP Beck, and GJM Velders. The effects of the conversion of nitrogen oxides in aircraft exhaust plumes in global models. *Geophysical Research Letters*, 24(23):3013–3016, 1997.

[28] EW Meijer, PFJ Velthoven, AM Thompson, L Pfister, H Schlager, P Schulte, and H Kelder. Model calculations of the impact of no x from air traffic, lightning, and surface emissions, compared with measurements. *Journal of Geophysical Research: Atmospheres*, 105(D3):3833–3850, 2000.

[29] Patrick Minnis, David F Young, Donald P Garber, Louis Nguyen, William L Smith, and Rabindra Palikonda. Transformation of contrails into cirrus during success. *Geophysical Research Letters*, 25(8):1157–1160, 1998.

[30] Ismo Napari, Madis Noppel, Hanna Vehkamäki, and Markku Kulmala. Parametrization of ternary nucleation rates for h2so4-nh3-h2o vapors. *Journal of Geophysical Research: Atmospheres*, 107(D19), 2002.

[31] R Paoli, D Cariolle, and R Sausen. Review of effective emissions modeling and computation, Geosci. Model Dev., 4, 643–667, doi: 10.5194, 2011.

[32] Roberto Paoli, Xavier Vancassel, François Garnier, and Philippe Mirabel. Large-eddy simulation of a turbulent jet and a vortex sheet interaction: particle formation and evolution in the near field of an aircraft wake. *Meteorologische Zeitschrift*, 17(2):131–144, 2008.

[33] Joyce E Penner. *Aviation and the global atmosphere: a special report of the Intergovernmental Panel on Climate Change.* Cambridge University Press, 1999.

[34] H Petry, J Hendricks, M Möllhoff, E Lippert, A Meier, A Ebel, and R Sausen. Chemical conversion of subsonic aircraft emissions in the dispersing plume: Calculation of effective emission indices. *Journal of Geophysical Research: Atmospheres*, 103(D5):5759–5772, 1998.

[35] J Picot, R Paoli, O Thouron, and D Cariolle. Large-eddy simulation of contrail evolution in the vortex phase and its interaction with atmospheric turbulence. *Atmospheric Chemistry and Physics*, 15(13):7369–7389, 2015.

[36] Hans R Pruppacher, James D Klett, and Pao K Wang. Microphysics of clouds and precipitation, 1998.

[37] Ernst Schmidt. Die entstehung von eisnebel aus den auspuffgasen von flugmotoren. *Schriften der Deutschen Akademie der Luftfahrtforschung, Verlag R. Oldenbourg, München, Heft 44*, 5(44):1–15, 1941.

[38] Ulrich Schumann. The impact of nitrogen oxides emissions from aircraft upon the atmosphere at flight altitudes—results from the aeronox project. *Atmospheric Environment*, 31(12):1723–1733, 1997.

[39] Ulrich Schumann. A contrail cirrus prediction model. *Geoscientific Model Development*, 5:543–580, 2012.

[40] Ulrich Schumann, F Arnold, R Busen, J Curtius, B Kärcher, A Kiendler, A Petzold, H Schlager, F Schröder, and K-H Wohlfrom. Influence of fuel sulfur on the composition of aircraft exhaust plumes: The experiments sulfur 1–7. *Journal of Geophysical Research: Atmospheres*, 107(D15), 2002.

[41] Ulrich Schumann, Paul Konopka, Robert Baumann, R Busen, T Gerz, H Schlager, P Schulte, and H Volkert. Estimate of diffusion parameters of aircraft exhaust plumes near the tropopause from nitric oxide and turbulence measurements. *Journal of Geophysical Research: Atmospheres*, 100(D7):14147–14162, 1995.

[42] Ulrich Schumann, H Schlager, F Arnold, R Baumann, Peter Haschberger, and O Klemm. Dilution of aircraft exhaust plumes at cruise altitudes. *Atmospheric Environment*, 32(18):3097–3103, 1998.

[43] Ulrich Schumann, Hans Schlager, F Arnold, J Ovarlez, H Kelder, Ø Hov, G Hayman, ISA Isaksen, J Staehelin, and Philip D Whitefield. Pollution from aircraft emissions in the north atlantic flight corridor: Overview on the polinat projects. *Journal of Geophysical Research: Atmospheres*, 105(D3):3605–3631, 2000.

[44] A Tabazadeh, OB Toon, and Patrick Hamill. Freezing behavior of stratospheric sulfate aerosols inferred from trajectory studies. *Geophysical Research Letters*, 22(13):1725–1728, 1995.

[45] Azadeh Tabazadeh, Eric J Jensen, and Owen B Toon. A model description for cirrus cloud nucleation from homogeneous freezing of sulfate aerosols. *Journal of Geophysical Research: Atmospheres*, 102(D20):23845–23850, 1997.

[46] MJ Tang, RA Cox, and M Kalberer. Compilation and evaluation of gas phase diffusion coefficients of reactive trace gases in the atmosphere: volume 1. inorganic compounds. *Atmospheric Chemistry and Physics*, 14(17):9233–9247, 2014.

[47] Owen B Toon and Richard C Miake-Lye. Subsonic aircraft: Contrail and cloud effects special study (success). *Geophysical Research Letters*, 25(8):1109–1112, 1998.

[48] HG Tremmel, H Schlager, P Konopka, P Schulte, F Arnold, M Klemm, and B Droste-Franke. Observations and model calculations of jet aircraft exhaust products at cruise altitude and inferred initial oh emissions. *Journal of Geophysical Research: Atmospheres*, 103(D9):10803–10816, 1998.

[49] Simon Unterstrasser and Klaus Gierens. Numerical simulations of contrail-to-cirrus transition–part 1: An extensive parametric study. *Atmospheric Chemistry and Physics*, 10(4):2017–2036, 2010.

[50] Simon Unterstrasser and Klaus Gierens. Numerical simulations of contrail-to-cirrus transition–part 2: Impact of initial ice crystal number, radiation, stratification, secondary nucleation and layer depth. *Atmospheric Chemistry and Physics*, 10(4):2037–2051, 2010.

[51] Simon Unterstrasser, Klaus Gierens, Ingo Sölch, and Martin Lainer. Numerical simulations of homogeneously nucleated natural cirrus and contrail-cirrus. part 1: How different are they? *Meteorologische Zeitschrift*, 26(6):621–642, 2017.

[52] Simon Unterstrasser, Klaus Gierens, and Peter Spichtinger. The evolution of contrail microphysics in the vortex phase. *Meteorologische Zeitschrift*, 17(2):145–156, 2008.

[53] Hanna Vehkamäki, Markku Kulmala, Ismo Napari, Kari EJ Lehtinen, Claudia Timmreck, Madis Noppel, and Ari Laaksonen. An improved parameterization for sulfuric acid–water nucleation rates for tropospheric and stratospheric conditions. *Journal of Geophysical Research: Atmospheres*, 107(D22), 2002.

[54] PF Vohralik, LK Randeniya, IC Plumb, and SL Baughcum. Effect of plume processes on aircraft impact. *Journal of Geophysical Research: Atmospheres*, 113(D5), 2008.

[55] Chowen C Wey, Bruce E Anderson, Changlie Wey, Richard C Miake-Lye, Philip Whitefield, and Robert Howard. Overview on the aircraft particle emissions experiment. *Journal of Propulsion and Power*, 23(5):898, 2007.

[56] JT Wilkerson, Mark Z Jacobson, Andrew Malwitz, Sathya Balasubramanian, R Wayson, G Fleming, AD Naiman, and SK Lele. Analysis of emission data from global commercial aviation: 2004 and 2006. *Atmospheric Chemistry and Physics*, 10(13):6391–6408, 2010.

[57] H-W Wong and RC Miake-Lye. Parametric studies of contrail ice particle formation in jet regime using microphysical parcel modeling. *Atmospheric Chemistry and Physics*, 10(7):3261–3272, 2010.

[58] J Zhao and RP Turco. Nucleation simulations in the wake of a jet aircraft in stratospheric flight. *Journal of Aerosol Science*, 26(5):779–795, 1995.